Exploring the Behavior of Materials: A Comprehensive Guide to Thermal Analysis and the Push for a Sustainable Future

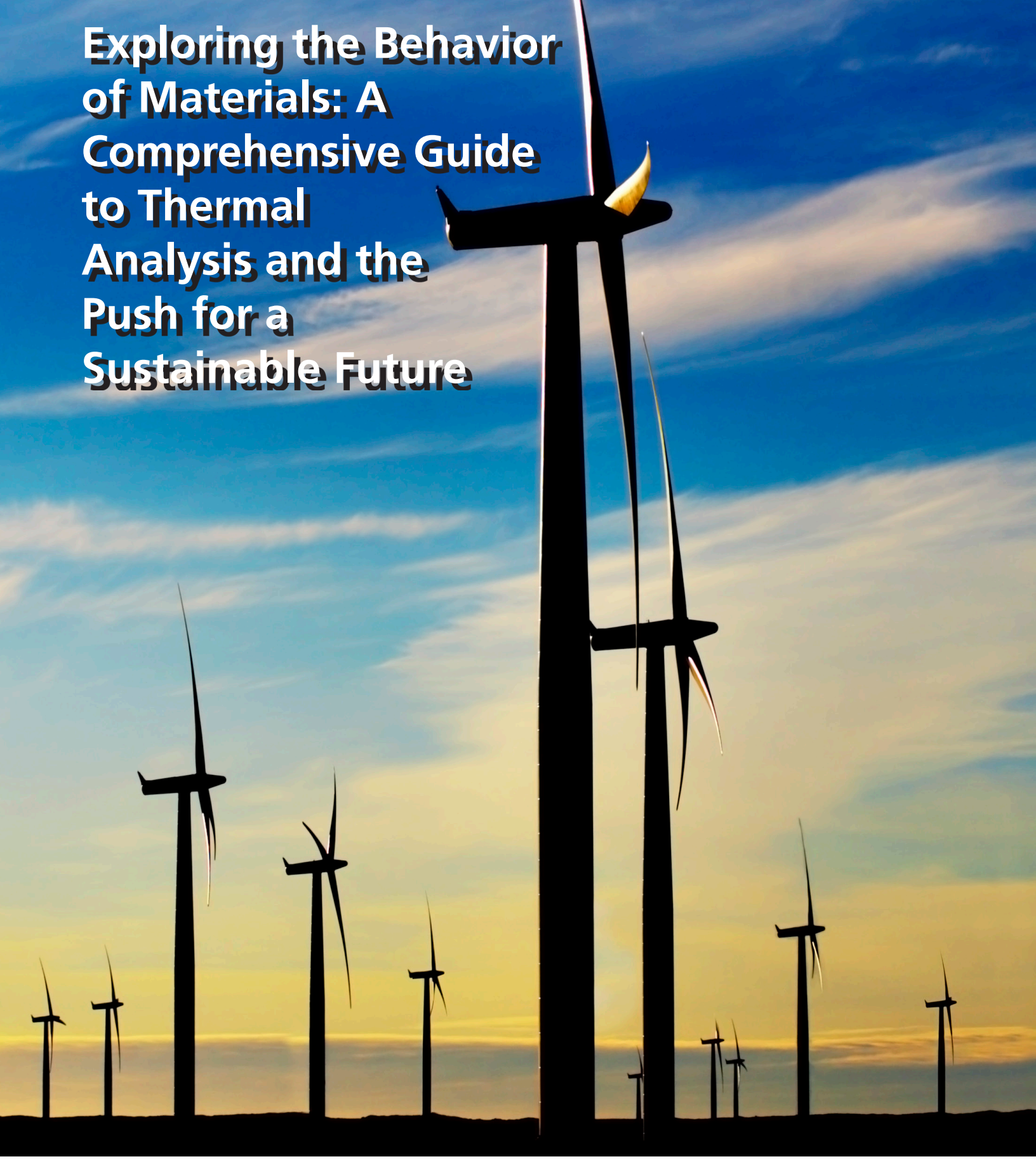

Sponsored by:

METTLER TOLEDO

WILEY Analytical Science

The DSC 5+ from METTLER TOLEDO
The New Standard in Differential Scanning Calorimetry

The DSC 5+ sets the new standard, delivering a superior performing and more productive DSC.

Find out more: www.mt.com/ta-dsc5plus

Features and benefits of the METTLER TOLEDO DSC 5+:

- **FlexMode™, choose power compensation or heat flux mode –** for optimal DSC performance
- **Power compensation –** provides outstanding resolution for separating close-lying effects
- **MultiSTAR™ sensor with 136 thermocouples –** exceptional sensitivity for the measurement of weak effects
- **Patented electrical heat flow adjustment –** saves time and ensures excellent measurement accuracy
- **Unrivalled modular concept –** tailor-made solutions for current and future needs
- **Time-saving FlexCal™ adjustment –** guarantees accurate results under all measurement conditions
- **Innovative robot with gas-purged crucible chamber –** protects samples from the environment and operates reliably around the clock

DSC Sensor Innovation

The DSC 5+ sensor with the FlexMode™ functionality can easily be switched between two different measurement modes. The robust and chemically resistant MMS 1 ceramic sensor provides a power compensation mode for excellent resolution and a heat flux mode for measurements that require high levels of sensitivity. This advanced sensor provides superior performance and allows the user to switch between modes to best suit the needs of the sample under investigation.

Contents

Imprint

111 River Street,
Hoboken, NJ 07030-5774
USA
Contact: Customer Service

Editor:
Róisín Murtagh

Senior Account Manager:
Joseph Tomaszewski

Mettler Toledo
mettlertoledo.com

Cover: © 2023 Adobe Stock

Introduction

Thermal analysis comprises a group of techniques used to study the behavior of materials as they are subjected to varying temperatures. It involves measuring and analyzing the physical and chemical changes that occur in a material as a result of heating or cooling. Differential Scanning Calorimetry (DSC) is widely used in thermal analysis to determine various thermodynamic properties of materials as they undergo these heating or cooling processes. It is a versatile tool that provides valuable information about sample transitions, such as phase changes, melting points, crystallization temperatures, glass transitions, and chemical reactions.

The principle of DSC is based on the measurement of the heat flow (ΔQ) that occurs when there is a thermal event in a sample. Two crucibles are placed on a sensor within a furnace, one is filled with the sample material in question, and the other is a reference crucible. The heat flow is then measured for the sample as the crucibles are subjected to a controlled temperature program. As the temperature increases, decreases or is held isothermally, the instrument measures the heat absorbed (endothermic effect) or released (exothermic effect) by the sample relative to the reference. This data is plotted as a function of temperature, producing a thermogram that represents the thermal properties of the material.

One of the significant advantages of DSC is its ability to provide quantitative information about heat flow and heat capacity, allowing for the determination of parameters such as specific heat capacity (c_p), and enthalpy (ΔH), of thermal temperatures (glass transition (T_g), melting and crystallization). These parameters can be vital in understanding the behavior and stability of many materials used in creating a more sustainable future, such as polymers that are used in lithium-ion battery thermal management and the manufacturing of the next generation wind turbine rotor blades.

This article collection begins with a study by Dong *et al.*[1], on the development of a phase change polymer (PCP) for use in battery thermal management. The PCP addresses challenges related to phase change material leakage, low heat dissipation capability, and reprocessability. By copolymerizing octadecyl acrylate (OA) and methyl methacrylate (MMA), the researchers achieved a PCP with intrinsic anti-leakage properties and improved heat dissipation. The PCP's rigid MMA segment ensures shape stability without requiring crosslinkers, enabling reprocessing. Additionally, the OA segments contribute chemical-bonded phase changeable side chains, delivering a high latent heat capacity and overcoming leakage issues.

In the next study, Bahiraei *et al.*[2], present a hybrid active-passive thermal management system for lithium-ion battery modules using phase change materials (PCM). Graphite nanopowder and highly oriented pyrolytic graphite sheets are used to improve the low thermal conductivity of the PCM. The thermophysical properties of the nano-enhanced PCM are experimentally explored. An electrochemical-thermal model is developed to analyze the thermal behavior of the battery module during a standard driving cycle. The results show that the hybrid system can effectively maintain the module temperature within safe limits and provide excellent temperature uniformity. Enhanced thermal conductivity is crucial for recovering the thermal energy storage capacity of the PCM. Overall, this cooling approach presents a promising solution for improved thermal management of Li-ion battery modules.

Finally, in a study by Schmidt *et al.*[3], five different binders used in the vacuum-assisted resin infusion process for manufacturing wind turbine rotor blades were characterized and evaluated. The solubility of these binders in a rotor-blade-proven epoxy resin was assessed, and the binders were classified into various categories based on their solubility. Mechanical and thermo-mechanical testing of resin-binder plates revealed that the strongly soluble binder Grilon MS performed the best, followed by the nonsoluble binder K-140 and the partially soluble binder D 2433E. Interply adhesion testing showed that peel strength differences were influenced by binder layer formations and binder-fiber interaction. The soluble binder Grilon MS exhibited the best overall performance and is expected to have the best mechanical performance in glass fiber-reinforced plastic laminates for wind turbine rotor blades.

Overall, thermal analysis is a versatile technique that delivers valuable results and generates new information in areas such as quality assurance and control, process and product development, and research.

Through the methods and applications presented in this article collection, we hope to educate researchers on innovative technologies for thermal analysis. For more information, we encourage you to visit Mettler Toledo to explore options to enhance your research.

Róisín Murtagh
Editor at *Wiley Analytical Science*

References

[1] Dong, X. et al. (2021). Preparation of Quasi-Thermoplastic Phase Change Polymer with Intrinsic Antileakage Performance for Battery Thermal Management. *Advanced Materials Interfaces.* DOI: 10.1002/admi.202100807.

[2] Bahiraei, F. et al. (2018). Electrochemical–Thermal Evaluation of an Integrated Thermal Management System for Lithium-Ion Battery Modules. *Advanced Theory and Simulations.* DOI: 10.1002/adts.201800021.

[3] Schmidt, S. et al. (2018). Powder binders used for the manufacturing of wind turbine rotor blades. Part 1. Characterization of resin-binder interaction and preform properties. *Polymer Composites.* DOI: 10.1002/pc.23988.

RESEARCH ARTICLE

ADVANCED MATERIALS INTERFACES

www.advmatinterfaces.de

Preparation of Quasi-Thermoplastic Phase Change Polymer with Intrinsic Antileakage Performance for Battery Thermal Management

Xinlong Dong, Binghe Zheng, Guoqing Zhang, Changren Xiao, and Xiaoqing Yang**

Phase change material (PCM) shows great potentials in battery thermal management (BTM) application, but there are significant challenges including PCM leakage, low secondary heat dissipation capability, and poor reprocessability. Herein, a type of phase change polymer (PCP) with intrinsic antileakage, reprocessability and heat dissipation capability is prepared via the copolymerization of octadecyl acrylate (OA) and methyl methacrylate (MMA). The rigid segment of MMA guarantees the shape stability of the PCP while avoiding using the crosslinkers, and thus simultaneously endows the linear PCP with quasi-thermoplastic property for reprocessing. The chemical-bonded phase changeable side chains from the OA segments provide a large latent heat of 100.5 J g^{-1} and fundamentally overcome the leakage problem. Additionally, the obtained PCP demonstrates a higher crystalline temperature favorable for secondary dissipation of the absorbed heat to the environment. Consequently, the obtained PCP demonstrates superior cooling performances in BTM applications. The temperature of the battery module with PCP cooling can be stably controlled below 52.5 °C under a harsh working environment of 3C-3C charge–discharge at 35 °C for 15 cycles. In contrast, the battery module adopting classical physically blended PCM cooling shows a much higher and gradually increasing maximum temperature during the cycles.

1. Introduction

In order to alleviate the crisis of fossil energy consumption and protect the ecological environment, pure electric vehicles (EVs) and hybrid EVs (HEVs) are promoted vigorously worldwide.[1–3] As the key component of EVs/HEVs, the thermal safety issues of the power battery pack in EVs/HEVs still bother the academic and industrial fields.[4–7] Thus, battery thermal management (BTM) systems are developed to strictly control the temperature rise and temperature difference (ΔT) with the aim of prolonging the lifespan of the battery module and avoiding thermal hazards.[8–11] Among various BTM systems, the passive temperature control technology based on phase change material (PCM) has been widely studied in recent years because of its simple installation and excellent cooling capability.[12–14]

Generally speaking, for engineering applications, pure PCMs are usually incorporated with thermal conductive agents like expanded graphite (EG) and form-stabilized components like polymer skeleton to overcome the poor thermal conductivity and enhance the shape stability after phase change occurs,[15–21] respectively. For example, Liu et al.[15] prepared a paraffin (PA)/EG/high-density polyethylene composite PCM (CPCM) and it exhibited well thermal stability and low PA leakage rate. Luo et al.[16] developed a PA/EG/epoxy resin-based CPCM and found that the EG and epoxy resin effectively enhanced the thermal conductivity and shape stability, respectively. Zou et al.[17] enhanced the thermal conductivity by constructing a multiwalled carbon nanotube/graphene thermal conductive skeleton. However, in such physically blended solid-liquid PCM (SLPCM), the phase change component (PCC) like PA gradually migrates and accumulates at the surface of the module during long-term and repeated use,[22,23] leading to a gradually decreasing cooling performance and raising the self-ignition risk of the module because most organic PCMs are easily combustible.[24–27] Although phase change microcapsules developed in recent years are believed to prevent PCM leakage theoretically,[28] the current strategy is still difficult to achieve a 100% overall-coating for the nano/microscale PCM microcapsules, and thus the leakage problem could not be fundamentally resolved.[29–31] Moreover, kilogram-leveled production of the microcapsules required by BTM application still remains a challenge.[32] In this context, we proposed a creative idea of designing a phase change polymer (PCP) with aliphatic side chains containing 18 carbon atoms in our previous work.[33] Not only the aliphatic side chains could provide a high latent heat of 98.8 J g^{-1}, but the chemical bonds between the main chain and the "PCC" of phase changeable side chains prevented the PCC migration and fundamentally overcame the leakage phenomenon.

However, in order to guarantee the shape stability of the PCPs, crosslinkers like divinyl benzene (DVB) and 1,6-hexanediol

X. Dong, B. Zheng, G. Zhang, C. Xiao, X. Yang
School of Materials and Energy
Guangdong University of Technology
Guangzhou 510006, P. R. China
E-mail: Xiaochangren@mail2.gdut.edu.cn; yangxiaoqing@gdut.edu.cn

The ORCID identification number(s) for the author(s) of this article can be found under https://doi.org/10.1002/admi.202100807.

DOI: 10.1002/admi.202100807

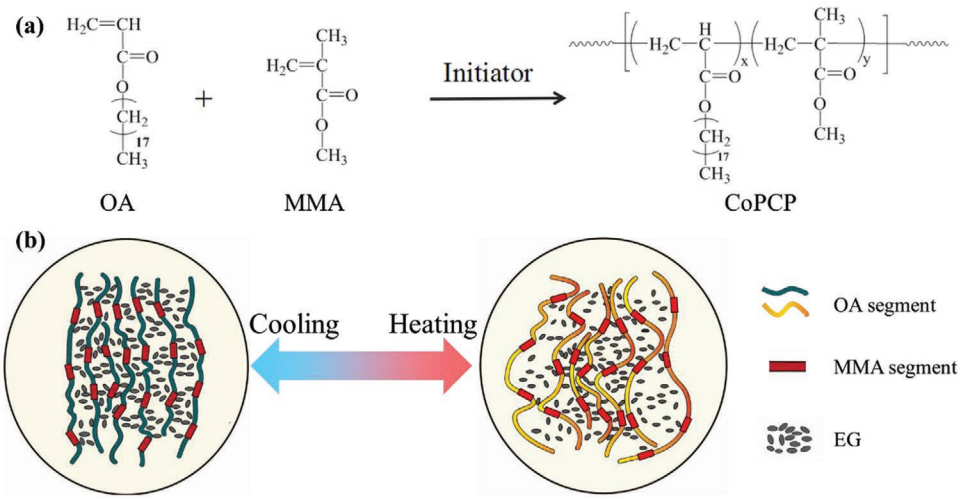

Figure 1. a) Synthetic mechanism of the CoPCP. b) Schematic diagram of the secondary procession capability of the quasi-thermoplastic CoPCP.

diacrylate (HDDA) were adopted, obtaining a crosslinking structure.[33] The crosslinking structure endows the PCP with well shape stability during operation. Unfortunately, the thermosetting property derived from such crosslinking structure requires a precise one-step forming of the PCP module and thus leads to a great application limitation because it is unfavorable to the flexible molding as well as the secondary processing of the PCP module into various specifications. Worse still, a relatively low crystalline temperature (T_c) is observed due to the confinement effect of the alkyl chains within the crosslinking polymer backbone, which makes it difficult to dissipate the absorbed heat during the exothermic process of the module, especially under the worst-case scenario like high ambient temperature in the summer of low latitudes areas.

To overcome these issues, in this work, we develop a new kind of quasi-thermoplastic PCP with a higher T_c through the copolymerization of the octadecyl acrylate (OA) and methyl methacrylate (MMA, **Figure 1**a) monomers. The rigid property of the MMA segment is able to guarantee the shape stability of the obtained copolymerized phase change copolymer (CoPCP) without using the crosslinkers, and simultaneously, the obtained linear CoPCP remains a quasi-thermoplastic property. EG is adopted as the thermal conductive fillers as usual and well-dispersed in the composite CoPCP. Compared to the thermosetting PCP/EG obtained in our previous work, this quasi-thermoplastic CoPCP/EG composite possesses a more flexible forming and secondary processing capability (Figure 1b) and can be molded into various modules with different specifications. In addition, the corresponding T_c of the obtained CoPCP shifts from 40.2 to 44.7 °C because the obtained comb-structured polymer allows a much freer nucleation/crystallization in comparison to the crosslinking molecular structure in the thermosetting PCP. This improvement undoubtedly benefits the secondary heat dissipation from the PCP module to the environment under high ambient temperatures. By employing this novel CoPCP, the 21 V/16 Ah battery module shows excellent reliability and reversibility: during the 15 loops of 3C-3C charge–discharge under a high ambient temperature of 35 °C, the CoPCP module demonstrates an excellent antileakage performance and the maximum temperature (T_{max}) of the CoPCP-based battery module can be stably controlled below 52.5 °C. On the contrary, the T_{max} of the thermosetting PCP-based and classical physically blended PCM-based battery modules demonstrates a gradually increasing trend and reaches 56.7 and 60.0 °C at the last loop without any ease trend, respectively. This is attributed to the aforementioned lower heat dissipation capability toward the environments resulting from the lower T_c, and the decreasing thermal energy storage capacity caused by the severe PCC leakage in the physically blended PCM module.[34]

2. Experimental Section

2.1. Materials

OA was provided by Guangzhou Hongcheng Biochemical Technology Co., Ltd. MMA, benzoyl peroxide (BPO) in the experimental group and DVB, HDDA in the reference group were supplied by Shanghai Macklin Biochemical Technology Co., Ltd. Diallyl terephthalate in the reference group was purchased from Shanghai Aladdin Biochemical Technology Co., Ltd. PA in the reference group was produced by Shanghai Joule Wax Co., Ltd. Low density polyethylene (LDPE) in the reference group with a density of 0.925 g cm^{-3} was purchased from Sinopec Shanghai petrochemical Co., Ltd. All of the reagents were used for PCM preparation without further processing. EG (average particle size: 150 µm, expansion ratio: 220 cm^3 g^{-1}) was prepared via an 850 °C heat-treatment of the natural flake graphite (Qingdao Tianyuanda Graphite Co., Ltd.) for 10 min. The pouch cells with lithium cobalt oxide cathode and graphite anode used to construct the battery modules were produced from Shenzhen Grepow Battery Co., Ltd.

2.2. Preparation of the CoPCP

OA and MMA monomers with a molar ratio of 1:10 were adopted to synthesize the quasi-thermoplastic CoPCP with not

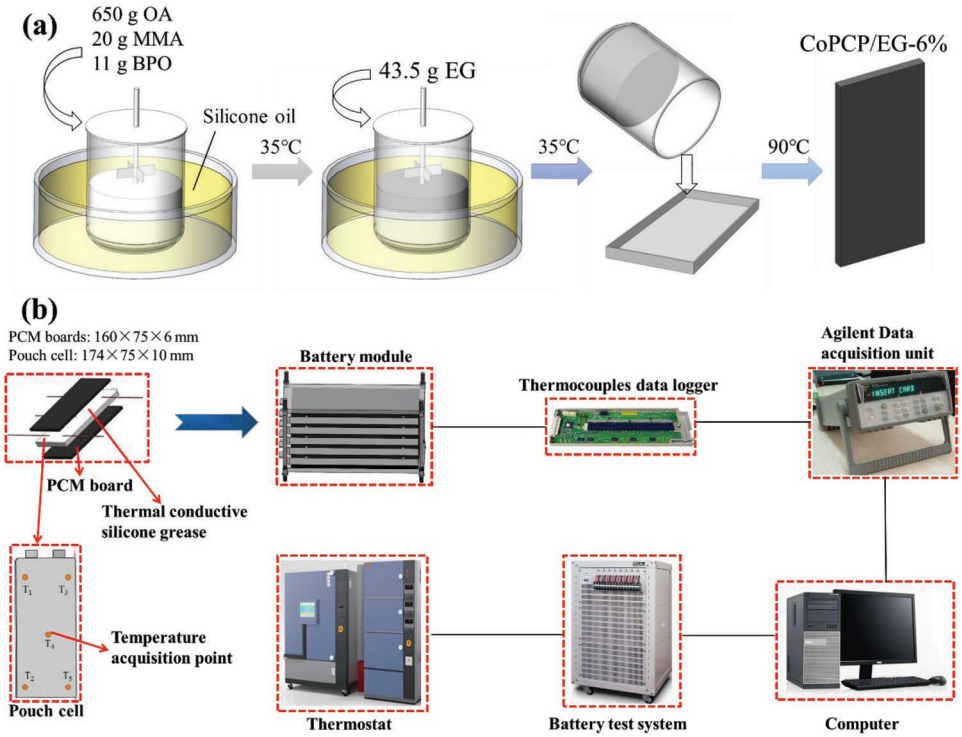

Figure 2. a) Preparation procedure of the CoPCP/EG-6%. b) Schematic diagram of the experimental system.

only excellent shape stability but high latent heat. In a typical synthesis process (**Figure 2**a), 650 g OA, 20 g MMA, and 11 g BPO were first added to the stainless steel vessel in succession, and then heated in a 35 °C-oil bath until a clear solution was formed. Subsequently, 43.5 g EG (mass fraction of 6 wt%) was gradually added under continuously mechanical stirring to obtain a homogeneously dispersed slurry. After that, the as-obtained precursors were poured into the steel/wood mold, transferred to a 90 °C-oven for 20 min, and then cooled to room temperature naturally for further demolding. Cylindrical specimens ($\Phi 36 \times 10$ mm^3) were prepared for shape stability and thermal conductivity tests. Rectangular specimens with dimensions of $75 \times 75 \times 5$ and $160 \times 75 \times 5$ mm^3 were prepared for antileakage tests and BTM tests, respectively. With the same procedures, two samples containing 8 and 10 wt% EG were also prepared. These CoPCP/EG composites with different EG contents were denoted as CoPCP/EG-*x*%, where *x* represented the mass percentage of the EG. As control groups, a classical physically blended PA/LDPE/EG ternary CPCM and a thermosetting PCP/EG composite with 6 wt% EG developed in the previous works were also prepared[22,33] and denoted as SLPCM/EG-6% and PCP/EG-6%, respectively.

2.3. Characterizations

Fourier transform infrared spectra (FTIR) of the monomers and CoPCP samples were measured by a Bruker Tensor II spectrophotometer with wavenumbers varying from 4000 to 500 cm^{-1}. Differential scanning calorimetry (DSC) curves were detected by a Mettler Toledo DSC3 differential scanning calorimeter from 0 to 80 °C with a heating rate of 10 °C min^{-1} under nitrogen atmosphere by using flake or powder like samples. X-ray diffraction (XRD) spectra were collected by a Rigaku Ultima III diffractometer equipped with a Cu K_α X-ray source at a scan rate of 8° min^{-1}. Thermal conductivity was measured by a Hotdisk 500 thermal constants analyzer, and the test temperature was 27 °C.

2.4. Thermal Stability and Leakage Tests

The shape stability test was carried out as follows: the samples were processed into cylinders with a diameter of 36 mm and a height of 6 mm. Then the cylinders were placed on a heating stage (JFTOOI 996D) and kept at 50, 70, 90, and 110 °C for 30 min successively.

The antileakage test was designed as follows: the rectangular SLPCM/EG-6% and CoPCP/EG-*x*% samples with a dimension of $75 \times 75 \times 6$ mm^3 were placed in a Bell BTH 80C programmable thermostat to simulate the repeated endothermic and exothermic process. In detail, the samples were heated to 70 °C for 1 h and then cooled to 30 °C for another 1 h. 100 cycles were executed. The mass retention of the samples was recorded by every five cycles.

3. Experimental Setup of the Battery Modules

To verify the feasibility of CoPCP/EG-*x*% in BTM applications, battery modules using PCM cooling (CoPCP/EG-6%, PCP/EG-6% and SLPCM/EG-6%) were constructed in a compact

Table 1. Parameters of the charge–discharge tests.

Process	Time [min]	Current	Voltage
Constant current charge	–	48 A (1 C)	Cutoff voltage of 21 V
Constant voltage charge	–	Cutoff current of 2 A	21 V
Rest	60	–	–
Constant current discharge	–	16–48 A (1–3 C)	Cutoff voltage of 15 V
Rest	60	–	–

sandwich structure consisting of six PCM boards and five pouch cells connected in series. To reduce the thermal contact resistance between the cells and the PCM boards, thermal conductive silicone grease was applied between the cells and the PCM boards. Figure 2b is the schematic diagram of the battery module and the experimental system. The battery module was charged–discharged using a Neware BTS-60 V/100 A battery test system under constant temperatures of 30 and 35 °C provided by a 1000 mm × 1000 mm × 1000 mm thermostat (Dongguan Bell BTH 1000 C). Omega J-type thermocouples (TT-J-30-SLE) were placed on the central surface of each cell. The temperature was recorded by an Agilent data acquisition unit. The battery module was first charged with a constant current mode at 3 C to 21 V (C-rate is the measurement of the charge and discharge current with respect to its nominal capacity) and then with a constant voltage mode at 21 V until the current dropped to 2 A. After rested for 60 min, the module was then discharged at 1, 2, or 3 C until the voltage dropped to 15 V. The charge–discharge protocols were denoted as *x*C-*y*C, where *x* and *y* represented the charge and discharge rates in the constant current mode, respectively. The detailed parameters are shown in **Table 1**.

4. Results and Discussion

4.1. Characterizations of the Obtained CoPCPs

As seen from the FTIR spectra from **Figure 3**a, all of the CoPCP samples demonstrate similar spectra containing a series of characteristic absorption peaks derived from the MMA and OA monomers. Owing to the asymmetric stretching vibration of C—H bonds of $-CH_3$ and $-CH_2-$, all the samples exhibit strong multiple absorption peaks at 2956, 2917, and 2850 cm^{-1}.[33] The absorption peak at 1731 cm^{-1} is assigned to the stretching vibration of the C=O double bond corresponding to the carboxyl group. The peaks in the region of 1475–1000 cm^{-1} correspond to the C—H in-plane bending vibration, stretch vibration of C—O bond and skeleton vibration of C—C single-bond.[28,35] It is noteworthy that the characteristic absorption peak of the C=C at 1635 cm^{-1} in OA and MMA disappears after copolymerization, suggesting the successful synthesis of the CoPCP.[36] The XRD patterns of the CoPCPs are displayed in Figure 3b. All of the samples exhibit a similar intense diffraction peak at 2θ of around 21.7°, indicative of the good crystalline derived from the C18 group, which can provide energy storage capacity during phase transition.[33] In addition, the intensity of the diffraction peak of EG at around 26.6° increases with the increase of EG ratio.

The DSC curves of the obtained CoPCPs are shown in **Figure 4** and the calculated latent heat (phase-change enthalpy, ΔH_m) are listed in **Table 2**. Similar curve shapes and phase change regions are observed during both the heating and cooling processes. These similar phase change behaviors are ascribed to the same components in the CoPCPs. As decreasing the mass fraction of the EG, the ΔH_m of the CoPCP/EG-*x*% increases, and the endothermic and exothermic peaks of the curve become narrower and sharper. Interestingly, peak separation phenomenon during the crystallization process is observed in all the CoPCP samples. This can be attributed to the different mobility of the alkyl chains resulting from the various lengths of the rigid MMA segments on the main chains via random copolymerization. As calculated, the ΔH_m of

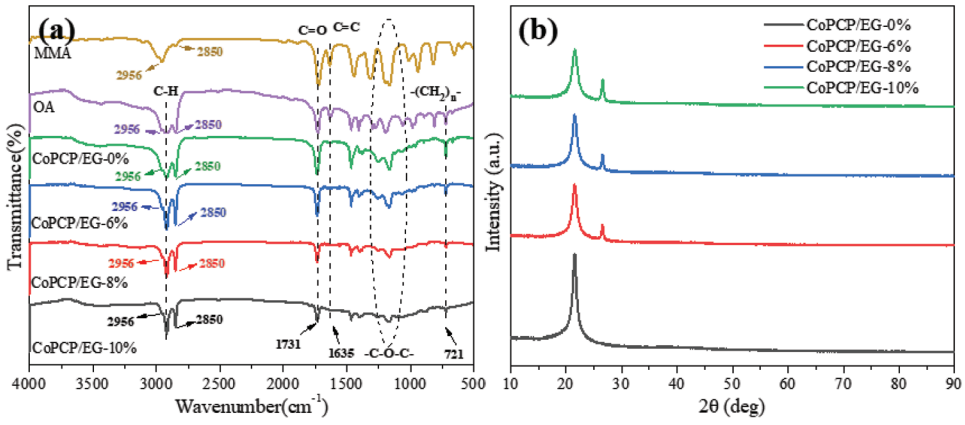

Figure 3. a) FTIR spectra and b) XRD patterns of the CoPCP/EG-*x*% samples.

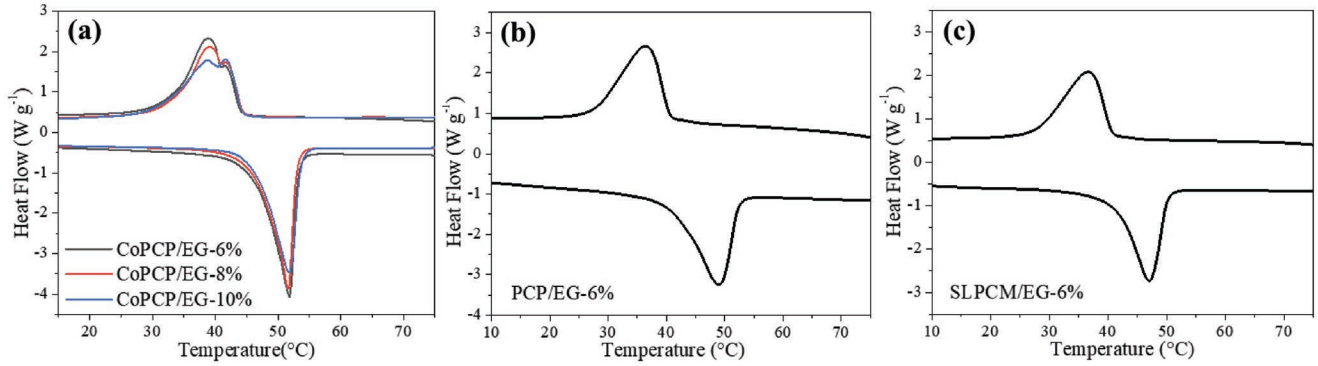

Figure 4. DSC curves of the a) CoPCP/EG-*x*%, b) PCP/EG-6%, and c) SLPCM/EG-6% samples.

CoPCP/EG-6%, CoPCP/EG-8%, and CoPCP/EG-10% is 100.5, 94.9, and 90.2 J g^{-1}, respectively. It should be noted that compared to the thermosetting PCP/EG-6%, the obtained CoPCP possesses a much higher T_c (44.7 vs 40.2 °C). This phenomenon could be ascribed to the different stacking patterns of alkyl groups (orthorhombic or hexagonal phase)[37] and the higher mobility of the alkyl chains within the linear molecular structure than the rigid crosslinking backbone.[38] Without doubt, the much higher T_c will play an important role in secondarily dissipating the absorbed heat toward the environment, avoiding excessive heat accumulation in the module, and thus ensuring a stable temperature control performance, especially under high ambient temperatures.

On the other hand, with the same EG content, the CoPCP/EG-6% and PCP/EG-6% demonstrate higher thermal conductivity than the classical SLPCM/EG-6% (Table 2), which is attributed to the in situ polymerization with the existence of EG, forming a homogeneous and continuous thermal conductive network in the PCP/EG-6% and CoPCP/EG-6%. Furthermore, the explosive polymerization phenomenon of the MMA segment inevitably results in some air existing in the obtained CoPCP/EG-6%, and therefore, the thermal conductivity of CoPCP/EG-6% (1.63 W m^{-1} K^{-1}) is lower than that of PCP/EG-6% (2.33 W m^{-1} K^{-1}). With the increase of the EG from 6 to 10 wt%, the thermal conductivity increases from 1.63 to 2.64 W m^{-1} K^{-1}. This increasing trend is consistent with the previous reports.[22,33] In addition, it is worth mentioning that the thermal conductivity and latent heat of the CoPCP/EG-*x*% are also higher than those of most previous reported CPCMs with various contents of the thermal conductive fillers (**Table 3**).

The most important attitude of designing PCP to replace conventional physically blended PCMs is to fundamentally solve the PCC leakage issue during long-term operations. **Figure 5**a shows the mass variations of the samples in the thermostat simulating 100 endothermic-exothermic cycles between 30 and 70 °C. Apparently, the classical physically blended SLPCM/EG-6% demonstrates a non-negligible mass loss during the simulating endothermic-exothermic process. During the cycles, the mass decreases from 27.85 to 24.41 g, suggesting that the LDPE/EG skeleton cannot completely hinder the migration of the PA. By stark contrast, the mass of all the CoPCP samples remains constant during the cycles. Undoubtedly, this excellent antileakage performance results from the chemical bonds between the main chain and phase changeable side chains, which fundamentally overcomes the migration of the PCC in traditional CPCMs.

The antileakage performance of the CoPCP samples was further confirmed by the stepwise heating tests. As seen in Figure 5b, when the temperature increases to 110 °C, the SLPCM/EG-6% sample collapses into liquid state mixture, and the lattice paper adsorbs a large amount of the molten PA and LDPE. Whereas, the CoPCP samples present excellent shape-stability, only showing slight shape change at 110 °C. Moreover, in comparison with the form-stable thermosetting PCP/EG-6%, the CoPCP/EG-*x*% samples soften without liquefaction as the temperature increases to 130 °C, and interestingly, after we remove the CoPCP specimens from the lattice paper, negligible adsorbed CoPCP is observed on the lattice paper. These aforementioned results prove that, the obtained CoPCPs possess a quasi-thermoplastic property and can be secondarily molded

Table 2. The tested and calculated results from the DSC and thermal conductivity tests.

Samples[a)]	T_m [°C]			ΔH_m [J g^{-1}]	Thermal conductivity [W m^{-1} K^{-1}]
	T_{mo}	T_{mp}	T_{me}		
SLPCM/EG-6%	41.75	47.40	51.63	116.14	1.47
PCP/EG-6%	41.62	47.31	51.23	95.34	2.33
CoPCP/EG-6%	47.14	52.09	54.23	100.50	1.63
CoPCP/EG-8%	46.85	50.90	52.87	94.90	2.04
CoPCP/EG-10%	46.11	51.16	53.51	90.20	2.64

[a)] T_m: melting temperature, T_{mo}: melting onset temperature, T_{mp}: melting peak temperature, T_{me}: melting endset temperature. "Melting" in the context refers to the solid–liquid phase change process of LPCM/EG-6% or CoPCP/EG-*x*% and solid–solid phase change process of PoPCM/EG-6%.

Table 3. Comparison of the latent heat and thermal conductivity of the CPCMs in previous works.

CPCM composition[a)]	Thermal conductive fillers (mass content)	Latent heat [J g^{-1}]	Thermal conductivity [W m^{-1} K^{-1}]	References
CoPCP/EG-6%	EG (6 wt%)	100.5	1.63	This work
1-Tetradecanol/Ag nanowire	Ag nanowire (62.73 wt%)	76.5	1.46	[39]
PA/GcN foam	GcN foam (29 wt%)	120.0	1.20	[40]
PA/EG/LDPE	EG (7 wt%)	81.7	≈1.30	[12]
PA/PPHFM/EG	EG (2 wt%)	100.2	0.35	[41]
SA/CNS	CNS (50 wt%)	91.8	0.43	[42]
PA/EG/POE	EG (7 wt%)	126.7	1.41	[4]
PA/EG/TPE	EG (5 wt%)	103.5	≈1.30	[43]
PA/EP/GP80	GP80 (10 wt%)	111.4	1.34	[44]

[a)]Abbreviations: Graphene coated nickel (GcN); polypropylene hollow fiber membranes (PPHFM); carbon nanospheres (CNS); polyolefin elastomer (POE); thermoplastic elastomer (TPE); graphite particle sizes of 80 (GP).

and easily recycled at higher temperatures, but still present excellent antileakage performance. For example, as shown in Figure 5c, two cylindrical CoPCP/EG-6% specimens turn to a shape-changeable quasi-liquid state at 200 °C and can be easily reprocessed into a rectangular shape within another rectangular mold after cooled to room temperature.

4.2. Temperature Control Performance of the CoPCP in BTM Application

From the above results, we know that the obtained CoPCPs possess suitable thermophysical properties and excellent antileakage performance for the practical application of BTM. Particularly, we anticipate that the higher T_c of the CoPCP may endow the whole module with a much-enhanced secondary heat dissipation capability, thereby reduces the heat accumulation inside the modules under high environment temperatures. Therefore, CoPCP/EG-6% was then molded into boards to construct the battery modules with five pouch cells and thereby its feasibility for BTM application was compared with PCP/EG-6% and classical SLPCM/EG-6%. For convenience, the battery modules coupled with CoPCP/EG-6%, PCP/EG-6% and SLPCM/EG-6% boards are abbreviated as the CoPCP module, PCP module, and SLPCM module, respectively.

Figure 6 compares the cooling performance of the SLPCM and CoPCP modules under a simulating harsh working condition, i.e., 3C-3C charge–discharge for 15 cycles under an ambient temperature of 30 °C. Obviously, although the SLPCM/EG-6% possesses a higher ΔH_m of 116 J g^{-1} than the CoPCP/EG-6%, its cooling capability is still lower than that of the CoPCP/EG-6%. For example, the T_{max} of the module is up to

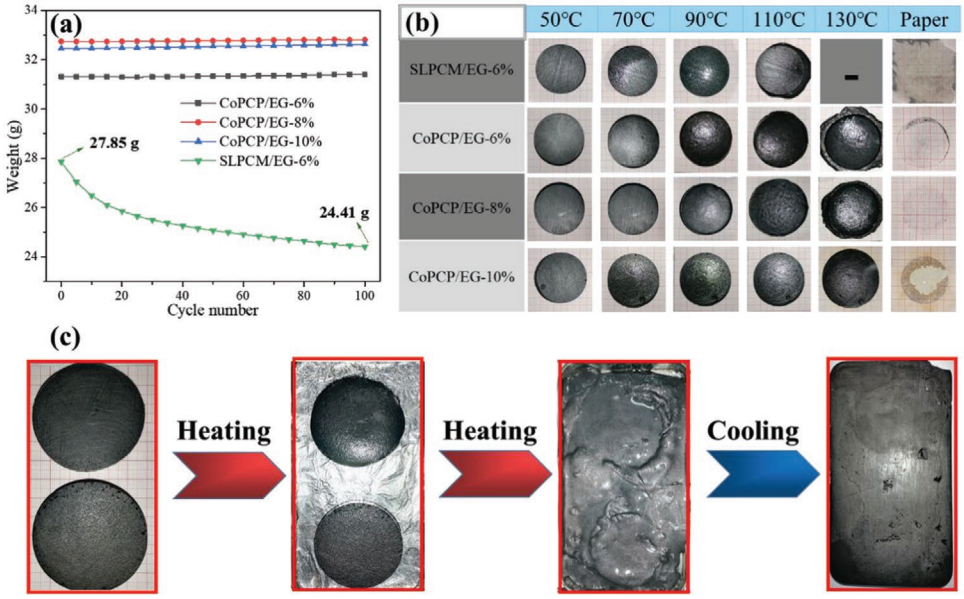

Figure 5. a) Mass variations of the samples in the thermostat simulating 100 endothermic–exothermic cycles. b) Photographs of the samples during the stepwise heating tests. c) Demonstration of the reprocessability of the quasi-thermoplastic CoPCP/EG-6% from cylindrical specimens into a rectangular specimen.

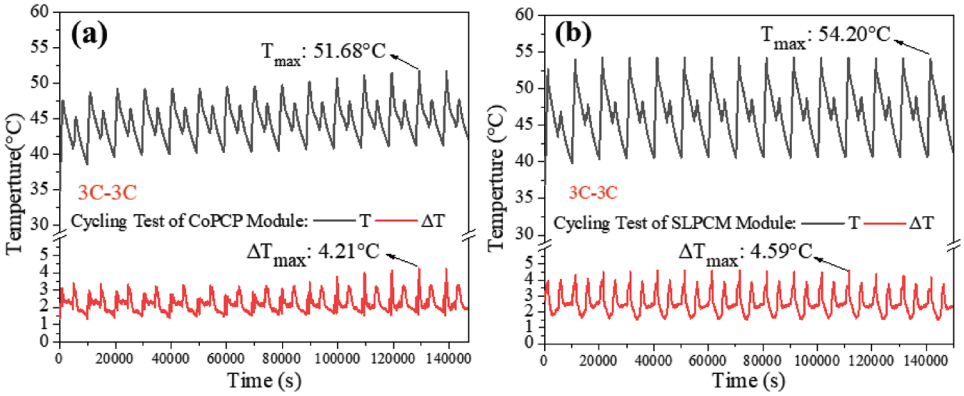

Figure 6. Temperature and ΔT variation curves of the of the a) SLPCM and b) CoPCP modules during 15 charge–discharge cycles under 30 °C.

54.6 °C, whereas that of the CoPCP module decreases greatly to 51.7 °C. Likewise, the maximum ΔT (ΔT_{max}) also shows similar characteristics with the T_{max}. The ΔT_{max} of the SLPCM and CoPCP modules is 4.6 and 4.2 °C, respectively.

As we mentioned above, the relatively low T_c of the PCP/EG-6% will undoubtedly lead to a heat accumulation phenomenon under relatively harsh working environments. When a high environmental temperature of 35 °C is provided (**Figure 7**a), heat accumulation phenomenon is clearly observed in the PCP module. During the charge–discharge process with different protocols of 3C-1C, 3C-2C, and 3C-3C, CoPCP/EG-6% and PCP/EG-6% show obvious cooling effect. For example, the T_{max} decreases by 2.3–3.5, 6.2–7.4, and 6.2–8.5 °C after coupling with the PCP or CoPCP boards. It is apparent that the

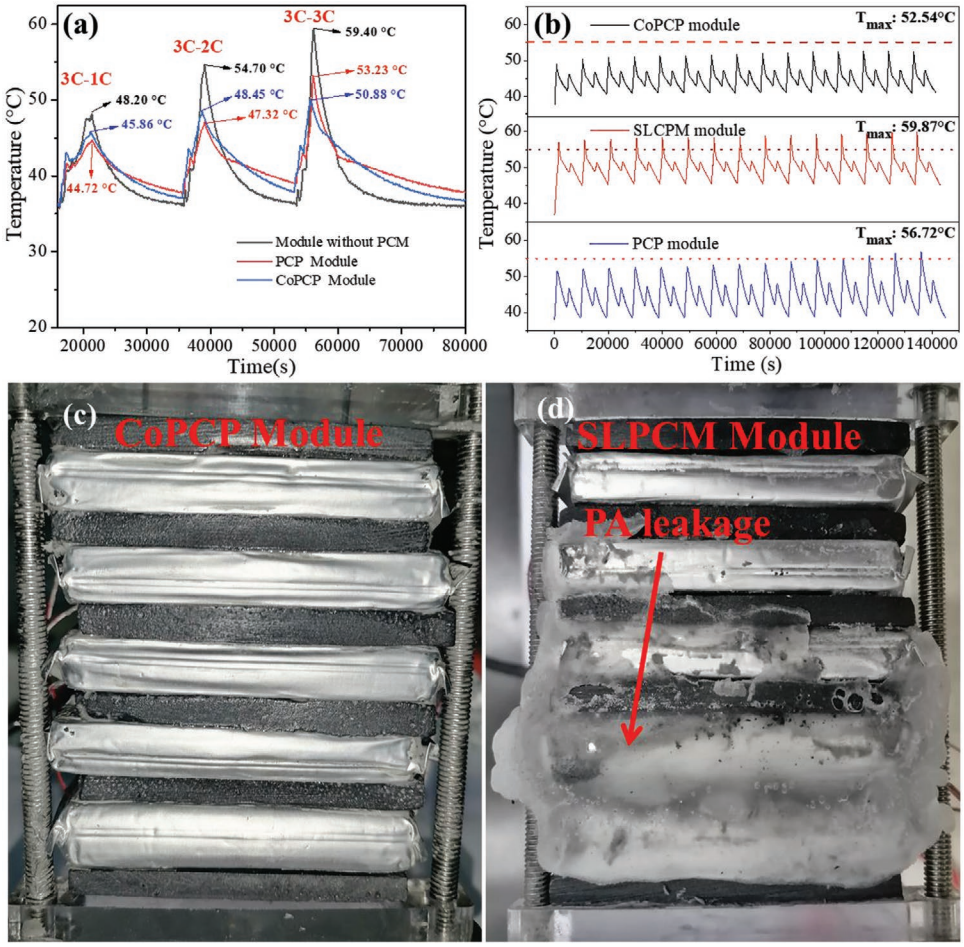

Figure 7. Temperature variation curves of the modules during a) the charge–discharge process with different protocols of 3C-1C, 3C-2C, and 3C-3C and b) 15 charge–discharge cycles under 35 °C. Comparison of the leakage phenomenon on the c) SLPCM and d) CoPCP modules.

Table 4. ΔH_m variations of the samples scraped from the SLPCM and CoPCP modules before and after the charge–discharge cycles.

Samples	ΔH_m [J g^{-1}]		Decline rate [%]
	Before cycling	After cycling	
SLPCM/EG-6%	116.1	75.1	35.3
CoPCP/EG-6%	100.5	100.0	0.5

temperature variation curves of the battery module without PCM cooling show the fastest cooling rate during the rest process, because the PCM module during the rest process plays a role in heat preservation. Interestingly, the cooling rate of the CoPCP module is also much faster than the PCP module. This phenomenon definitely proves the better heat dissipation capability of the CoPCP with a higher T_c from the boards to the environment.

As expected, this advantage becomes more remarkable during the cycling tests at 3C-3C. Under such a harsh working environment (Figure 7b), the T_{max} of the CoPCP module is about 3–5 °C lower than that of the PCP module. More importantly, during the 15 charge–discharge cycles at 3C-3C, the T_{max} of the PCP module increases gradually without an ease trend owing to the relatively low heat dissipation performance. For example, the T_{max} in the 1st, 5th, 10th, and 15th cycle is 51.3, 52.3, 54.1, and 56.7 °C, respectively. By stark contrast, due to the higher secondary heat dissipation capability originating from the higher T_c, the T_{max} of the CoPCP module reaches a stable state at 52.5 °C after the 11th cycle.

On the other hand, the classical SLPCM module delivers the worst cooling performance, possessing the highest T_{max} accompanying with an increasing trend as well. Besides the relatively lower T_c, the leakage of PCC existing in such physically blended CPCM is undoubtedly another important reason. As shown in Figure 7c, after the charge–discharge cycles in 35 °C, PA participates onto the module surface, and thus accumulates into PA bulks. To our delight, the surface of the CoPCP module remains clean without obvious trace of leakage (Figure 7d). The comparison of the DSC tests of the samples scraped from the PCM modules before and after cycling quantitatively concludes that the ΔH_m of the SLPCM/EG-6% decreases from 116.1 to 75.1 J g^{-1}, whereas that of the CoPCP/EG-6% stays constant at about 100 J g^{-1} (**Table 4**). Overall, this new kind of quasi-thermoplastic PCP realizes the flexible and secondary processing of the module, while guaranteeing the excellent antileakage property and cooling performance in BTM application.

5. Conclusion

We have successfully prepared a novel kind of CoPCP through the copolymerization of OA and MMA. The obtained CoPCP shows great applicability for BTM application based on the following advantages: first, the rigid MMA segment guarantees the shape stability of the CoPCP without using the crosslinkers, and thereby the obtained linear structure of the CoPCP possesses a quasi-thermoplastic property, which is beneficial to the flexible forming and secondary reprocessability. Second, the chemical-bonded phase changeable side chains derived from the OA segments provide a large latent heat of 100.5 J g^{-1} as well as an intrinsic antileakage characteristic for the CoPCP. Third, the much higher T_c of the CoPCP is favorable to dissipating the absorbed heat to the environment. As a result, the CoPCP demonstrates a stable and great cooling performance compared to the classical physically blended CPCM. For instance, under a harsh working environment, i.e., 15 charge–discharge cycles of 3C-3C at 35 °C, the T_{max} of the battery module with CoPCP can be controlled below 52.5 °C, which remains stable after the 11th cycle. For comparison, the classical SLPCM module shows a gradually increasing value of the T_{max} during the charge–discharge cycles.

Acknowledgements

This work was supported by the Natural Science Foundation of Guangdong Province (2019A1515011525) and National Natural Science Foundation of China (NNSFC, 21875046).

Conflict of Interest

The authors declare no conflict of interest.

Data Availability Statement

Research data are not shared.

Keywords

battery thermal management, copolymerization, phase change material leakage, thermoplastic properties

Received: May 18, 2021
Revised: July 5, 2021
Published online: August 27, 2021

[1] M. Safdari, R. Ahmadi, S. Sadeghzadeh, *Energy* **2020**, *193*, 116840.
[2] F. M. Eltoumi, M. Becherif, A. Djerdir, H. S. Ramadan, *Renewable Sustainable Energy Rev.* **2021**, *138*, 110534.
[3] W. Wu, S. Wang, W. Wu, K. Chen, S. Hong, Y. Lai, *Energy Convers. Manage.* **2019**, *182*, 262.
[4] X. Zou, J. Liu, *Energy Rep.* **2020**, *6*, 2948.
[5] D. P. Finegan, M. Scheel, J. B. Robinson, B. Tjaden, I. Hunt, T. J. Mason, J. Millichamp, M. Di Michiel, G. J. Offer, G. Hinds, D. J. L. Brett, P. R. Shearing, *Nat. Commun.* **2015**, *6*, 6924.
[6] D. Ouyang, J. Weng, J. Hu, M. Chen, Q. Huang, J. Wang, *Thermochim. Acta* **2019**, *676*, 205.
[7] J. Xu, J. Chao, T. Li, T. Yan, S. Wu, M. Wu, B. Zhao, R. Wang, *ACS Cent. Sci.* **2020**, *6*, 1542.
[8] H. Liu, Z. Wei, W. He, J. Zhao, *Energy Convers. Manage.* **2017**, *150*, 304.
[9] W. Zichen, D. Changqing, *Renewable Sustainable Energy Rev.* **2021**, *139*, 110685.
[10] M. Mashayekhi, E. Houshfar, M. Ashjaee, *Appl. Therm. Eng.* **2020**, *178*, 115543.
[11] R. Jilte, A. Afzal, S. Panchal, *Energy* **2021**, *219*, 119564.

[12] Y. Lv, W. Situ, X. Yang, G. Zhang, Z. Wang, *Energy Convers. Manage.* **2018**, *163*, 250.
[13] Z. Sun, R. Fan, F. Yan, T. Zhou, N. Zheng, *Int. J. Heat Mass Transfer* **2019**, *145*, 118739.
[14] Z. Rao, Y. Wen, C. Liu, *Particuology* **2018**, *41*, 85.
[15] Z. Liu, J. Huang, M. Cao, G. Jiang, Q. Yan, J. Hu, *Appl. Therm. Eng.* **2021**, *185*, 116415.
[16] X. Luo, Q. Guo, X. Li, Z. Tao, S. Lei, J. Liu, L. Kang, D. Zheng, Z. Liu, *Renewable Energy* **2020**, *145*, 2046.
[17] D. Zou, X. Liu, R. He, S. Zhu, J. Bao, J. Guo, Z. Hu, B. Wang, *Energy Convers. Manage.* **2019**, *180*, 1196.
[18] R. Kizilel, R. Sabbah, J. R. Selman, S. Al-Hallaj, *J. Power Sources* **2009**, *194*, 1105.
[19] Z. Ling, J. Chen, X. Fang, Z. Zhang, T. Xu, X. Gao, S. Wang, *Appl. Energy* **2014**, *121*, 104.
[20] Z. Rao, Q. Wang, C. Huang, *Appl. Energy* **2016**, *164*, 659.
[21] S. Wu, T. Li, Z. Tong, J. Chao, T. Zhai, J. Xu, T. Yan, M. Wu, Z. Xu, H. Bao, T. Deng, R. Wang, *Adv. Mater.* **2019**, *31*, 1905099.
[22] Y. Lv, X. Yang, X. Li, G. Zhang, Z. Wang, C. Yang, *Appl. Energy* **2016**, *178*, 376.
[23] J. Zhang, X. Li, G. Zhang, Y. Wang, J. Guo, Y. Wang, Q. Huang, C. Xiao, Z. Zhong, *Energy Convers. Manage.* **2020**, *204*, 112319.
[24] W. Luo, C. Lyu, L. Wang, L. Zhang, *J. Power Sources* **2013**, *241*, 295.
[25] C.-V. Hémery, F. Pra, J.-F. Robin, P. Marty, *J. Power Sources* **2014**, *270*, 349.
[26] Z. Wang, J. Wang, *Energy* **2020**, *204*, 117946.
[27] S. Wu, T. Li, M. Wu, J. Xu, Y. Hu, J. Chao, T. Yan, R. Wang, *J. Mater. Chem. A* **2020**, *8*, 20011.
[28] Z. Sun, K. Sun, H. Zhang, H. Liu, D. Wu, X. Wang, *Sol. Energy Mater. Sol. Cells* **2021**, *225*, 111069.
[29] X. Meng, S. Qin, H. Fan, Z. Huang, J. Hong, X. Xu, X. Ouyang, D.-Z. Chen, *Sol. Energy Mater. Sol. Cells* **2020**, *212*, 110589.
[30] S. Lashgari, A. R. Mahdavian, H. Arabi, V. Ambrogi, V. Marturano, *Eur. Polym. J.* **2018**, *101*, 18.
[31] J. Y. Do, N. Son, J. Shin, R. K. Chava, S. W. Joo, M. Kang, *Mater. Des.* **2021**, *198*, 109357.
[32] J. Chen, S. Kang, J. E. , Z. Huang, K. Wei, B. Zhang, H. Zhu, Y. Deng, F. Zhang, G. Liao, *J. Power Sources* **2019**, *442*, 227228.
[33] C. Xiao, G. Zhang, Z. Li, X. Yang, *J. Mater. Chem. A* **2020**, *8*, 14624.
[34] T. Ma, L. Li, Q. Wang, C. Guo, *J. Mater. Sci.* **2018**, *54*, 875.
[35] Z. Yang, Y. Deng, J. Li, *Appl. Therm. Eng.* **2019**, *150*, 967.
[36] Y. Mao, J. Gong, M. Zhu, H. Ito, *Polymer* **2018**, *150*, 267.
[37] H. Wang, X. Han, H. Shi, X. Zhang, L. Qi, D. Wang, *CrystEngComm* **2014**, *16*, 7090.
[38] L. Zhang, H. Shi, W. Li, X. Han, X. Zhang, *Polym. Int.* **2014**, *63*, 982.
[39] L. Ianniciello, P. H. Biwolé, P. Achard, *J. Power Sources* **2018**, *378*, 383.
[40] A. Hussain, I. H. Abidi, C. Y. Tso, K. C. Chan, Z. Luo, C. Y. H. Chao, *Int. J. Therm. Sci.* **2018**, *124*, 23.
[41] D. Luo, L. Xiang, X. Sun, L. Xie, D. Zhou, S. Qin, *Energy* **2020**, *197*, 117252.
[42] M. Mehrali, S. Tahan Latibari, M. Mehrali, T. M. I. Mahlia, H. S. Cornelis Metselaar, *Energy Convers. Manage.* **2014**, *88*, 206.
[43] Z. Cai, J. Liu, Y. Zhou, L. Dai, H. Wang, C. Liao, X. Zou, Y. Chen, Y. Xu, *Sol. Energy Mater. Sol. Cells* **2021**, *219*, 110728.
[44] X. Zuo, X. Zhao, J. Li, Y. Hu, H. Yang, D. Chen, *Sol. Energy* **2020**, *209*, 85.

FULL PAPER

Lithium-Ion Batteries

ADVANCED THEORY AND SIMULATIONS

www.advtheorysimul.com

Electrochemical–Thermal Evaluation of an Integrated Thermal Management System for Lithium-Ion Battery Modules

Farid Bahiraei, Maryam Ghalkhani, Amir Fartaj, and Gholam-Abbas Nazri*

Thermal management of lithium-ion (Li-ion) batteries using phase change materials (PCM) demonstrate advantages such as compactness and reduced weight compared to conventional active cooling systems. However, the heat accumulation in PCM due to ineffective cooling and added thermal inertia may lead to thermal management system failure. In this study, a hybrid active–passive thermal management system for a Li-ion battery module is presented. Graphite nanopowder and highly oriented pyrolytic graphite sheets are employed to improve the low thermal conductivity of the PCM. The thermophysical properties of the nano-enhanced PCM (NePCM) with various mass fractions are experimentally explored. A streamlined electrochemical–thermal coupled model for batteries is used to develop an air-assisted hybrid thermal management system model. The effects of nanoparticles mass fraction, thickness of the PCM layer, and air inlet temperature on the module thermal behavior during a standard driving cycle are investigated. The hybrid system can maintain the module temperature within the safe limits and provide excellent temperature uniformity. The results reveal that an enhanced thermal conductivity is essential to recover the thermal energy storage capacity of PCM during the driving cycle. The proposed cooling approach presents a promising avenue for enhanced thermal management of Li-ion battery modules.

1. Introduction

Electric vehicles (EV) and hybrid electric vehicles (HEV) are considered the best near-term candidates to reduce the greenhouse gas emission in the transportation sector. Rechargeable lithium-ion (Li-ion) batteries have high specific energy and energy density relative to other cell chemistries which makes them well-suited for electrification of vehicles. The main barriers to the use of Li-ion batteries in electrical/hybrid vehicles are safety, cost related to cycle and calendar life, and low-temperature performance.[1] These challenges are strongly coupled with the thermal effects in the battery. Furthermore, in case of overcharging, a Li-ion battery may undergo thermal runaway and explode due to decomposition of the battery components that generate flammable gas species. In addition, heating the battery outside a specific range can accelerate the battery aging and sever capacity fading. Therefore, the goal of battery thermal management system (BTMS) is to increase the lifetime of Li-ion cells by moderating the operating temperature of the cell.

There are two major strategies for thermal management in electric vehicles: an active method by using air or a liquid as coolant[2,3] or a passive approach by employing phase change materials (PCM).[4,5] Air cooling can moderate the batteries temperature rise, but in aggressive driving cycles and/or at high operating temperatures it will result in a large non-uniform temperature distribution in the battery module.[6–8] This leads to different capacity fading rates for each cell, and as a result the life cycle of the whole pack reduces. Efforts into optimizing the flow channels to improve the temperature uniformity increase the system complexity and cost.[9,10] Liquid cooling with water, oil, or refrigerants as the heat-transfer medium shows higher thermal efficiency due to the higher heat capacity of liquids compared to air.[11] Various liquid cooling BTMS has been investigated in many studies.[3,12–15] However, these systems require a sophisticated flow pattern and consume more energy and space due to the presence of condenser, evaporator, and pumps.

The PCM cooling for BTMS was first introduced by Al-Hallaj and Selman[16] in which the PCM absorbs the heat generated by Li-ion batteries and keeps the temperature of the batteries within their melting range. It has been showed that PCM cooling systems benefit from many advantages such as high compactness, low cost, no need for circulatory network, better performance in case of thermal run away, and more uniform temperature distribution.[17–19] Despite these, there are some drawbacks in this method such as low thermal conductivity of PCM,

Dr. F. Bahiraei, Prof. A. Fartaj
Department of Mechanical
Automotive and Materials Engineering
University of Windsor
Windsor, Ontario N9B3P4, Canada
E-mail: bahirae@uwindsor.ca
Dr. M. Ghalkhani
Department of Electrical and Computer Engineering
University of Windsor
Windsor, Ontario N9B3P4, Canada
Prof. G.-A. Nazri
Electrical and Computer Engineering Department
Wayne State University
Detroit, MI 48202, USA

DOI: 10.1002/adts.201800021

insufficient heat rejection during aggressive operation, and unfavorable thermal inertia.

A serious concern in PCM-based BTMS is the limited latent heat storage of these materials. In extreme conditions such as high battery heat generation and/or high ambient temperature, the PCM may run out of available latent heat and fail to control the battery module temperature.[20] Furthermore, the lack of efficient heat rejection from the module may also result in thermal management system failure due to the high thermal inertia of PCM. These challenges may tackle through two main approaches, that is, enhancing the thermal conductivity of the based-PCM, or increasing the external heat release by utilizing fins or forced convection.

Various methods are proposed to enhance the thermal conductivity of the PCM.[21] The addition of highly conductive carbon-based nanoparticles is considered as an effective approach to increase the thermal conductivity of PCM due to their low densities and intrinsic high thermal conductivities.[22] Enhancing the PCM thermal conductivity will result in a more uniform temperature distribution which can improve the heat rejection from the module to the ambient.

Employing forced air convection to improve the performance of a passive BTMS has been rarely reported in the literature. Fathabadi[23] numerically modeled a battery pack consisting of 20 battery units with 19 distributed ducts and layers of paraffin/expanded graphite as the PCM. This hybrid system with varied convective heat transfer coefficients showed better performance than a similar air-cooled system at various ambient temperatures. Ling et al.[24] reported an investigation of a power battery cooling system by using an organic PCM/expanded graphite with forced-air cooling system under constant current charge/discharge cycles. The results revealed that the forced-air cooling system is important to maintain the batteries temperature within the safe limit.

Numerical thermal management investigations in the module and pack levels mentioned above were performed by lumped thermal models with heat generation data obtained from experiments. This is due to the significant computational cost required for 3D coupled electrochemical–thermal models. However, an accurate assessment of batteries thermal responses to cooling scenarios needs 3D coupled electrochemical–thermal models. Numerical studies on the integrated BTMS are commonly conducted during constant current discharge or discharge. Nevertheless, electric and hybrid electric vehicles driving cycles, and consequently batteries charge/discharge cycles, present complex patterns that cannot be precisely modeled with constant current discharge rates.

In the current work, a fast simulation 3D coupled electrochemical–thermal modeling approach for Li-ion batteries along with the experimental validation of the electrical and thermal responses are presented. Furthermore, two paraffin/graphite nanopowder composite is synthesized and its temperature-dependent thermophysical properties are characterized experimentally. The nanocomposites as well as highly oriented pyrolytic graphite (HOPG) plates are employed in an Li-ion battery module to provide a novel integrated thermal management system. The numerical model uses a 3D coupled electrochemical–thermal simulation approach to assess the batteries thermal behavior during a standard hybrid electric vehicle driving cycle. The performance of the proposed thermal management system is evaluated under various cooling system design parameters, air inlet temperature, and nanocomposite formulations.

2. Experimental Section

2.1. Battery Behavior

The variation of open-circuit voltage (OCV) and surface temperature of the battery were measured under various discharge rates ranging from 0.5C to 4C. Thermal imaging was used to record the temperature distribution on the battery surface utilizing an infrared (IR) camera. The camera resolution is 640 × 480 pixels with an accuracy of ±0.01 K. During the experiments, the battery was mounted inside a constant-temperature chamber to ensure uniform natural convection heat transfer from all sides.

2.2. Preparation of Nanocomposites

An industry-grade paraffin wax with a nominal melting point (T_m) of 333.15 K was adopted as the base PCM. The graphite nanopowder was purchased from MK Impex Corp., Ontario, Canada. The materials were used as received without further purification in all experiments. The nanoparticles at desired weights were added to the melted PCM at 90 °C and intensively stirred for 30 min to provide a homogeneous mixture. A temperature higher than the PCM melting point was preferred as a relatively low viscosity of the molten PCM facilitates the dispersion of the nanoparticles. A very small amount of PolyVinylPyrrolidone-40 (Sigma-Aldrich, Oakville, Canada) was added to the mixture as a dispersing additive to assure a good dispersion of the nanoparticles in the liquid PCM. Finally, the liquid composite was rigorously sonicated at about 90 °C for 2 h prior to the solvent evaporation. Two samples with different weight fractions of 5 and 10 wt% were prepared. The thermophysical properties of the materials used in this study are listed in **Table 1**.

2.3. Thermophysical Characterization of Nanocomposites

The thermal conductivity of nano-enhanced PCM (NePCM) composites were measured with a C-Therm TCi thermal conductivity analyzer (accuracy better than 5%) using modified transient plane source (MTPS) technique. In each measurement, the solid sample was initially heated to a temperature higher than its melting temperature inside a chamber. The liquid sample was then allowed to solidify onto the sensor surface to assure a uniform thermal contact between the sample and the sensor surface.

The heat capacity, latent heat of fusion, and melting temperature of the NePCM were determined using a differential scanning calorimeter (Mettler-Toledo DSC822). A sample size of around 15–20 mg was loaded to the DSC cell and the data was collected for the second run at a rate of 3 K min^{-1}.

The dynamic viscosity of the liquid nanocomposite samples was measured using a rotational viscometer (Brookfield LVT,

Table 1. Thermophysical properties of the materials used in this study.

Property	Paraffin wax	CNF	GNP	Graphite nanopowder
Melting point [K]	333.15	–	–	–
Thermal conductivity [W m^{-1} K^{-1}]	Solid: 0.25 Liquid: 0.16	–	–	–
Specific heat [J kg^{-1} K^{-1}]	Solid: 1180 Liquid: 2056	–	–	–
Density [kg m^{-3}]	910	2100	100	2200
Dynamic viscosity [mPa s]	5.5	–	–	–
Latent heat [kJ kg^{-1}]	119.3	–	–	–
Characteristic length	–	OD: 400 nm Length: 50 μm	Thickness: 7 nm APS: 15 μm	APS: 50 nm

Table 2. Governing equations and boundary conditions used in the battery electrochemical–thermal model.[25]

Physics	Governing equation and boundary conditions
Mass balance in liquid phase	$\varepsilon_l \frac{\partial c_l}{\partial t} + \nabla \cdot \left(-D_l^{\text{eff}} \nabla c_l + \frac{i_l t_+}{F} \right) = \frac{S_a j_n}{F}$
	$D_l^{\text{eff}} = D_l \, \varepsilon_l^{\gamma_l}$
Mass balance in solid phase	$\frac{\partial c_s}{\partial t} - \frac{1}{r^2} \frac{\partial}{\partial r} \left(r^2 D_s \frac{\partial c_s}{\partial r} \right) = 0$
	$\frac{\partial c_s}{\partial r} = 0 \text{ at } r = 0$
Ionic transport in liquid phase	$i_l = -\sigma_l^{\text{eff}} \nabla \Phi_l + \frac{2RT\sigma_l^{\text{eff}}}{F} \left(1 + \frac{\partial ln f_{\pm}}{\partial ln c_l} \right) (1 - t_+) \nabla (ln c_l)$
	$\sigma_l^{\text{eff}} = \sigma_l \, \varepsilon_l^{\gamma_l}$
	$\frac{\partial c_l}{\partial x} = 0 \text{ at } x = L_{\text{NCC}} \text{ and } x = L_{\text{NCC}} + L_N + L_s + L_P$
Electron transport in solid phase	$\nabla \cdot i_s + \nabla \cdot i_l = 0$
	$\nabla \cdot i_s = -S_a j_n$
	$i_s = -\sigma_s^{\text{eff}} \nabla \Phi_s$
	$\sigma_s^{\text{eff}} = \sigma_s \, \varepsilon_s^{\gamma_l}$
	$-\sigma_s^{\text{eff}} \nabla \Phi_s = 0 \text{ at } x = L_{\text{NCC}} + L_N \text{ and } x = L_{\text{NCC}} + L_N + L_s$
Electrochemical kinetics	$j_n = j_0 \left\{ \exp\left(\frac{\alpha_a F}{RT} \eta \right) - \exp\left(-\frac{\alpha_c F}{RT} \eta \right) \right\}$
	$j_0 = F k_0 c_l^{\alpha_a} (c_{s,\max} - c_{s,\text{surf}})^{\alpha_a} c_{s,\text{surf}}^{\alpha_c}$
	$\eta = \Phi_s - \Phi_l - U_{\text{eq}}$
	$U_{\text{eq}} = U_{\text{eq,ref}} + \frac{\partial U_{\text{eq}}}{\partial T} (T - T_{\text{ref}}), \quad T_{\text{ref}} = 293.15 \text{ K}$

Cooksville, Canada) with an accuracy of 1% at elevated temperatures from about 333 to 363 K at an increment of 10 K. Temperature control during viscosity measurements was performed using a constant-temperature bath.

3. Numerical Modeling

3.1. Battery Electrochemical–Thermal Model

A fast simulation pseudo 3D electrochemical–thermal model suitable for thermal analysis was used in this study. The model was based on the coupling of mass, charge, and energy conservations, as well as electrochemical kinetics. The current numerical approach uses a 1D local electrochemical cell unit to find the reaction and polarization heat generations as well as the electrolyte concentration distribution in the active battery material. The values of concentration are inserted in a 3D electric current conservation solver to calculate the distributed ohmic heat generation. Finally, the 3D energy conservation equation is solved to find the temperature distribution considering three heat generation contributions from anode, cathode, and the electrolyte phases. The pseudo 3D model described above is adapted for a 5 Ah nickel cobalt aluminum oxide (NCA) battery. The governing equations, basic parameters of the battery, and the module in simulations are listed in **Table 2**,[25] **Table 3**,[26,27] and **Table 4**. The OCV and voltage–temperature coefficient of porous electrodes are obtained from literature.[25–27]

Table 3. Parameters used in the battery electrochemical–thermal model.[26,27]

Parameter	Al CC	Cathode	Electrolyte	Anode	Cu CC
c_0 [mol m^{-3}]	–	33956	1000	31507	–
c_p [kJ kg^{-1} K^{-1}]	900	1250	1518	1437	385
D [m^2 s^{-1}]	–	1.5E−15	[a]	[b]	–
E_{aD} [kJ mol^{-1}]	–	18	–	4	–
E_{aR} [kJ mol^{-1}]	–	3	–	4	–
F [C mol^{-1}]	–	–	96487.332	–	–
k [W m^{-1} K^{-1}]	160	1.38	0.099	1.04	400
k_0 [m$^{2.5}$ mol$^{-0.5}$ s^{-1}]	–	3.255E−11	–	1.764E−11	–
r_0 [μm]	–	1.2	–	14.75	–
t_+	–	–	0.363	–	–
α_a, α_c	–	0.5	–	0.5	–
δ [μm]	23	46	26	48	16
ε	–	0.423	0.4	0.56	–
ρ [kg m^{-3}]	2700	4740	1210	5031	8960
σ [S m^{-1}]	3.8E7	91	[c]	100	6.3E7

[a] $\log(D_l) = -(4.43 + \frac{54}{T-229-0.005\times c_l} + 0.0022 \times c_l)$; [b] $D_s = [3.9 \times 10^{-14}(1.5 - \mathrm{SOC})^{3.5}] \exp[\frac{E_{aD}}{R}(\frac{1}{T_{ref}} - \frac{1}{T})]$; [c] $\sigma_l(c_l, T) = 1.2544 \times 10^{-4} c_l \times (0.22002 \times 10^{-6} {c_l}^2 + 0.26235 \times 10^{-3} c_l - 0.1765 \times 10^{-9} {c_l}^2 T + 0.93063 \times 10^{-5} c_l T + 0.8069 \times 10^{-9} c_l T^2 - 0.2987 \times 10^{-5} T^2 - 8.2488)$.

Table 4. Specifications of the battery and module used in simulations.

Parameter	Value
Battery width [mm]	80
Battery height [mm]	110
Battery thickness [mm]	9
Battery capacity [Ah]	5
Battery tab dimensions [mm]	15 × 10 × 0.5 ($w \times h \times t$)
Cooling channel height, h [mm]	6
PCM layer thickness, t [mm]	1, 2, 3
HOPG sheet thickness [mm]	1
Cooling channel width, w [mm]	505, 515, 525
Coolant inlet temperature [K]	293.15

3.2. Battery Module Cooling System Configuration

A 1.3 kWh battery pack consisted of 12 modules is considered. Each module contains six 5 Ah NCA Li-ion batteries in parallel. **Figure 1** shows the schematic of the proposed hybrid battery cooling system with two air-cooling channels. Two PCM layers are used between adjacent cells to improve the temperature uniformity of the batteries by absorbing their heat generation at a relatively constant temperature as shown in Figure 1. A thin sheet of HOPG is inserted in PCM layers to improve the heat conduction of the cooling channels and enhance temperature uniformity in the module. The performance of the proposed cooling system is tested under federal urban driving cycle (FUDC) for hybrid electric vehicles.

The temperature distribution in Li-ion batteries is not symmetrical due to different thermal and electrical conductivities of positive (aluminum) and negative (copper) tabs. Therefore, in this study, the cooling systems are numerically modeled by a half of the module with symmetry boundaries on the outer side of one of the PCM layers.

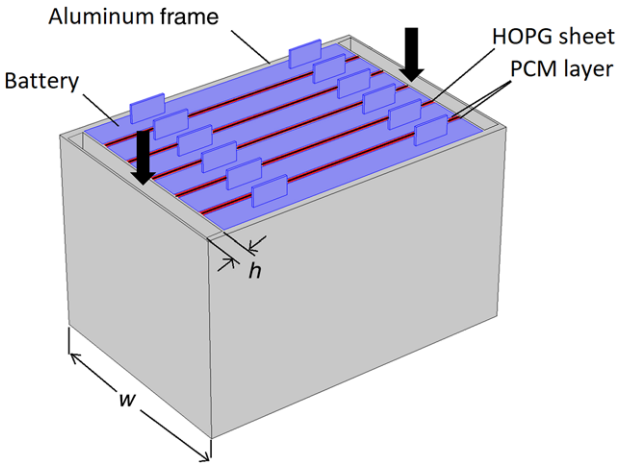

Figure 1. Schematic of hybrid cooling system and the direction of air flow.

3.3. Air Flow

Air is considered as the coolant and the flow is assumed to be laminar in all cases due to the low flow velocity and short characteristic lengths in this work. The mass conservation equation of air in the cooling channel is

$$\nabla \cdot \boldsymbol{u} = 0 \tag{1}$$

The momentum conservation equation of the coolant is as follows:

$$\rho_a \frac{\partial \boldsymbol{u}}{\partial t} + \rho_a (\boldsymbol{u} \cdot \nabla)\boldsymbol{u} = \nabla \cdot \left[-p\boldsymbol{I} + \mu\left(\nabla \boldsymbol{u} + (\nabla \boldsymbol{u})^T\right.\right. \tag{2}$$

where ρ_a is the density of air and $\boldsymbol{u}$ is the velocity vector of air in the cooling channel.

The energy conservation equation for air is

$$\frac{\partial}{\partial t}\left(\rho_a C_{p_a} T_a\right. + \nabla \cdot \left(\rho_a C_{p_a} \boldsymbol{u} T_a\right. - \nabla \cdot (k_a \nabla T_a) = 0 \tag{3}$$

where T_a is the temperature of air, and k_a and C_{pa} are the thermal conductivity and specific heat of air, respectively.

Three initial temperatures of 20, 30, and 40 °C are used. The initial temperature of the batteries is equal to the air inlet temperature, which implies that the air at ambient temperature is utilized in BTMS. Velocity and pressure boundary conditions are used for the coolant at inlet and outlet boundaries, reactively. A no-slip boundary condition is used on all internal cooling channel walls. Heat insulation boundary condition is defined at all external boundaries of the battery module.

3.4. Heat Transfer in NePCM

The flow of liquid NePCM is assumed unsteady, laminar, Newtonian, and incompressible.[28] It is also assumed that the melted nanocomposite behaves as a continuous medium with thermodynamic equilibrium and no slip velocity between the base PCM and solid nanoparticles. The thermophysical properties of the melted NePCM are assumed constant except the density variation in the buoyancy term which is modeled by the Boussinesq approximation.[29] In the simulations, the specific heat of PCM samples are defined based on the DSC curves.

The NePCM samples densities are calculated as follows[30]:

$$\rho_{\mathrm{NePCM}} = (1-\phi)\,\rho_{\mathrm{PCM}} + \phi\rho_{\mathrm{np}} \tag{4}$$

where ρ_{np} is the density of the nanoparticles and ϕ is the mass fraction.

The governing equations used in the transient laminar natural convection flow are as follows:
Continuity:

$$\nabla \cdot \boldsymbol{u} = 0 \tag{5}$$

Momentum:

$$\rho_{\mathrm{NePCM}} \frac{\partial \boldsymbol{u}}{\partial t} + \rho_{\mathrm{NePCM}} (\boldsymbol{u}\cdot\nabla)\,\boldsymbol{u} = \nabla \cdot \left[-p\boldsymbol{I} + \mu\left(\nabla\boldsymbol{u} + (\nabla\boldsymbol{u})^T\right.\right.$$
$$\left.\left. + \boldsymbol{g}\beta\,(T - T_{\mathrm{ref}})\right.\right. \tag{6}$$

where β is the thermal expansion coefficient of PCM samples.
Energy:

$$\left(\rho C_{\mathrm{p\ NePCM}} \frac{\partial T}{\partial t} + \left(\rho C_{\mathrm{p\ NePCM}} \boldsymbol{u}\cdot\nabla T + \nabla\cdot(-k_{\mathrm{NePCM}}\nabla T) = 0\right.\right. \tag{7}$$

The boundary and initial conditions are as follows:

$$u = w = z = 0 \quad \text{at walls} \tag{8}$$

$$q'' = -k_{\mathrm{NePCM}} \frac{\partial T}{\partial n} \quad \text{at battery surfaces} \tag{9}$$

$$\frac{\partial T}{\partial z} = 0 \quad \text{at module top and bottom surfaces} \tag{10}$$

$$T_{(x,y,z)} = T_{\mathrm{ini}} \quad \text{at } t = 0 \tag{11}$$

The simultaneous governing equations are solved using COMSOL Multiphysics v5.2 based on the finite element method. The specific heat of nanocomposites in the solid and mushy phases are defined as functions of temperature based on values obtained from the DSC measurements and the thermal conductivity in the mushy phase is estimated using a linear interpolation function.

The mesh independency is checked to ensure reliability of the simulation results. In all module designs, free quadrilateral mesh is used at the boundaries with the swept method along the battery thickness direction. The number of elements has been varied from about 750 000 to 1 400 000. The mesh independency study shows that the module temperature distribution is mesh-independent when the number of total elements is more than about 1 050 000. Therefore, this mesh design is used in the simulations. A two-way approach is used to couple the electrochemical and thermal solvers. The heat generation contributions are first calculated based on the derived values from electrochemical solver at a constant temperature. Then, the thermal solver uses the battery heat generation to find the temperature distribution in the module. The average of temperature will be used in the battery electrochemical solver in the next time step.

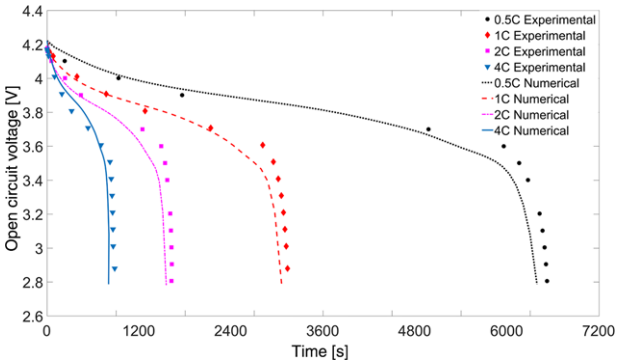

Figure 2. Open circuit voltage simulation and experimental results.

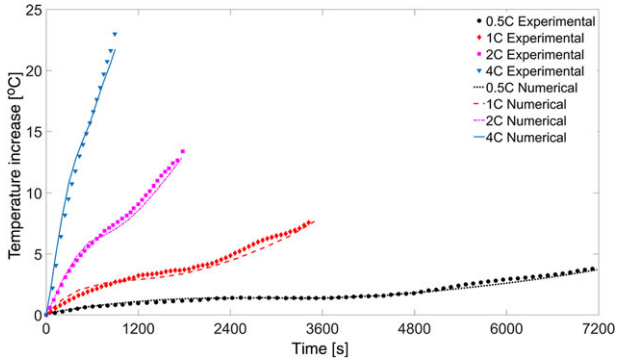

Figure 3. Temperature increase simulation and experimental results.

4. Results and Discussion

4.1. Battery Model

The experimental and simulated results of OCV and temperature increase are presented in **Figures 2** and **3**, respectively. Figure 2 depicts the battery OCV under 0.5C, 1C, 2C, and 4C discharge rates. The numerical results agree well with the experimental data. The anode and cathode OCV data are not measured values from the battery under study, but they are obtained from the literature[25–27] which may cause the differences between numerical and experimental values as observed in Figure 2. The measured and calculated values of average temperature increase are shown in Figure 3 under various discharge rates. The inconsistency between recorded and predicted values is more considerable at the end of 4C discharge rate due to higher ohmic heat generation from the contact resistance at battery tabs. The penetration of this heat from the tabs into the active material may cause the differences between the experimental and numerical

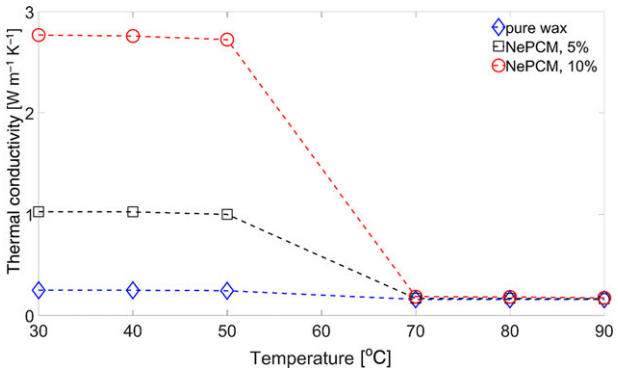

Figure 4. Thermal conductivity of PCM samples as a function of mass fraction of nanoparticles and temperature.

Table 5. Average thermal conductivity of pure paraffin and nanocomposites.

Sample	Thermal conductivity, solid/liquid [W m^{-1} K^{-1}]
Paraffin wax	0.25/0.16
5 wt% nanocomposite	1.02/0.17
10 wt% nanocomposite	2.75/0.18

values of the battery temperature increase. Both the OCV profile and the temperature rise of the simulation compare well with the experimental data which indicates that the modeling approach can simulate the real battery accurately.

4.2. Nanocomposite Thermophysical Properties

Figure 4 shows the thermal conductivity of the pure paraffin and nanocomposites as functions of temperature and concentration. The thermal conductivity of samples at temperatures close to the melting point (60 °C) are not shown due to the non-equilibrium state of the materials at this temperature, which may result in inaccurate measurements.[31] This figure shows that the thermal conductivity increases with the nanoparticle concentration and it drops during the melting. As can be seen from this figure, the thermal conductivity of the melted nanocomposites ($T > 60$ °C) cannot be considered a strong function of temperature or concentration in the liquid phase. During the solidification process, nanoparticles may trap in the wax crystalline structures, which increases the stress on the nanoparticles and enhances the effective contact area between the nanoparticle–wax intersections. The internal stress on the nanoparticles is released during the melting and reduces the inter-particle contact area that is observed as a reduction in thermal conductivity enhancement in the liquid phase. The average solid and liquid phase thermal conductivity of the samples are presented in **Table 5**.

Figure 5a shows the results of the DSC analysis of NePCM samples at various mass concentrations. The melting and freezing processes of the composites are demonstrated by the upper and lower curves, respectively. It seems that the melting point of paraffin wax does not change considerably by adding different nanoparticles. The enthalpies are calculated by integration the

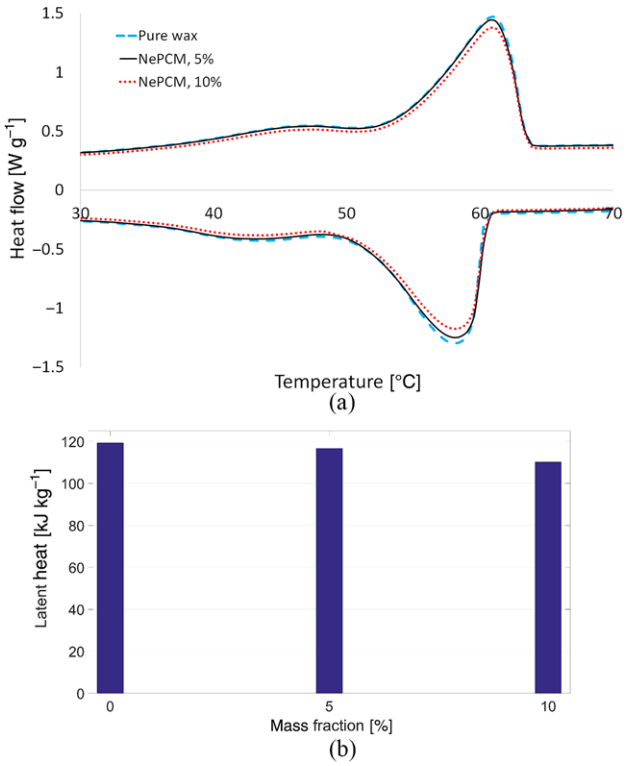

Figure 5. a) DSC heating and cooling curves of various PCM samples. b) Phase change enthalpy PCM samples as a function of mass fraction of nanoparticles.

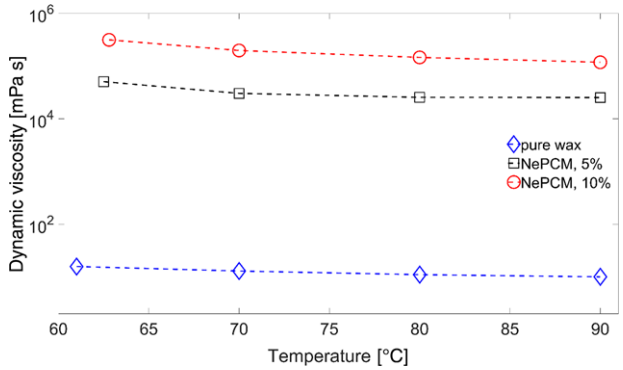

Figure 6. Dynamic viscosity of PCM samples as a function of mass fraction and temperature.

peaks above the baseline by the DSC software and are compared in Figure 5b. The NePCM latent heats of fusion are degraded compared to pure wax because of the accumulative replacement of the paraffin wax with nanoadditives.

The measured viscosities of the various nanocomposites are presented in **Figure 6**. As shown in this figure, the values of viscosity increase drastically with nanoparticles concentration. The measured values of viscosity decrease with temperature and the reduction becomes more noticeable at both higher temperatures and concentrations.

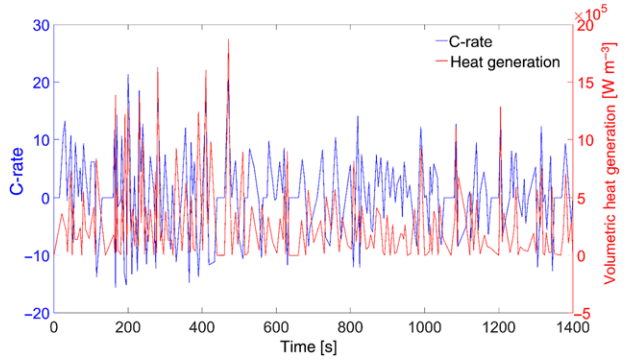

Figure 7. Variation of batteries C-rate and heat generation during the driving cycle.

4.3. PCM-Based Cooling System

In this section, the simulations are performed under HEV FUDC.[32] The FUDC is applied to the described battery pack to evaluate the variation of batteries C-rate with time. The pseudo 3D battery model is employed into each cooling system to assess their impact on the battery module performance under the driving cycle. In particular, the effects of the air inlet temperature, nanoparticles mass fraction, thickness of PCM layer on average, and local module temperatures are explored.

In this study, an initial value of SOC = 70% is used in all simulations.[33,34] **Figure 7** shows the variation of a battery C-rate and volumetric heat generation during the driving cycle. In this figure, the positive and negative values of C-rate correspond to the discharge and charge of the battery, respectively. High charge and discharge currents, as shown in Figure 7, generate a considerable amount of heat in the batteries which shows the necessity of an effective cooling strategy.

The module temperature distribution with different PCM at the end of the driving cycle is shown in **Figure 8**. The cooling plates and channels, as well as the battery tabs are not shown so that the temperature distribution along the battery thickness can be observed clearly. In all cases, the maximum temperature occurs at the center of the module because the inner battery is surrounded by two heat-generation sources which result in more heat accumulation and consequently more temperature non-uniformity. **Table 6** presents the maximum and average temperatures during the driving cycle. In this table, battery 1 represents the battery close to the module exterior wall and battery 3 is the inner battery close to the symmetry boundary condition. Utilizing a higher nanoparticle mass fraction only slightly reduces both maximum and average battery temperatures. This cooling system configuration cannot provide a relatively uniform temperature distribution in the module as the heat conduction from the batteries to the cooling air is not sufficient. Further enhancement of the proposed thermal management system is discussed in the following section.

The melted fraction of pure PCM, 5, and 10 wt% nanocomposites at the end of the driving cycle are 83%, 71%, and 56%, respectively. The melted fraction decreases with the nanoparticles loading due to the higher thermal conductivity of the composites. This shows an advantage of nanocomposites compared to the pure wax since it may lead to a prolonged temperature control capability.

Adding nanoparticles has two main effects on the base PCM: it increases the solid phase thermal conductivity and decreases the latent heat. The improved temperature distribution at higher mass fraction implies that the main reason of large temperature non-uniformity in the module is the low heat conduction. Therefore, attempts to improve the current design should focus on enhancing the effective thermal conductivity in the module.

4.4. PCM/HOPG-Based Cooling System

In order to enhance the heat conduction in the battery module, a HOPG sheet with extremely high thermal conductivity is adopted as a heat spreader. HOPG sheets covered in two layers

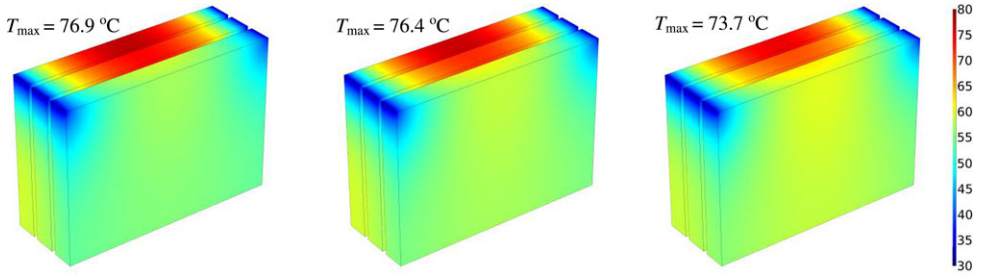

Figure 8. Temperature distribution in the module without HOPG sheet using pure wax (left), 5 wt% NePCM (center), and 10 wt% NePCM (right) at the end of the driving cycle.

Table 6. The maximum and average battery temperatures.

PCM	Battery 1, temperature maximum/average [°C]	Battery 2, temperature maximum/average [°C]	Battery 3, temperature maximum/average [°C]
Pure wax	66.8/52	81.6/56.1	83.9/57.4
Nanocomposite, 5 wt%	65.5/51.1	79.6/55.6	82.4/57.2
Nanocomposite, 10 wt%	64.6/50.2	78.3/55.0	81.7/69.0

Table 7. Thermophysical properties of HOPG.

Property	Value
Density [kg m^{-3}]	2300
Specific heat [J kg^{-1} K^{-1}]	730
Thermal conductivity [W mK^{-1}]	In plane: 1600
	Out of plane: 8

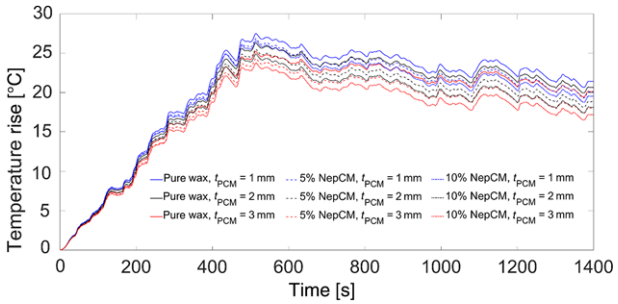

Figure 9. Variation of batteries average temperature under various PCM layer thickness.

of PCM (Figure 1) are used to transport heat out of the module through conduction, and then to reject it to the cooling air. HOPG sheets are highly conductive, flexible, chemically inert, and non-corrosive, which make them promising materials for effective thermal management of compact electric devices. The thermophysical properties of the commercial HOPG used in this study are shown in **Table 7**.

4.4.1. Effects of PCM Layer Thickness

A series of simulations is conducted to evaluate the effects of PCM layer thickness on the thermal performance of the proposed BTMS. All simulations have the same initial and air inlet temperature (30 °C) and are conducted for a HOPG sheet thickness equal to 1 mm. Three values of PCM layer thickness namely 1, 2, and 3 mm are investigated. Any change in the thickness of plates will change the cooling channel hydraulic diameter, and consequently, the Reynolds number. In order to evaluate the effect of cooling plate thickness, the inlet velocity is appropriately modified to keep the Reynolds number at a constant value of 1000 in all cases.

Figure 9 shows the variation of module average temperature rise (the average temperature of all three batteries) with time for three PCM samples at various thicknesses. As can be seen from the figure, for each sample, the average temperature decreases with the thickness of the PCM layer. When a thicker layer is used, both latent heat capacity and heat transfer area between the PCM and the cooling channels increase which lead to a lower average battery temperature.

For a constant PCM layer thickness, utilizing the nanoparticles can reduce the batteries temperature due to more heat conduction to the cooling channels. Quantitative analysis shows that using a 2 mm thick layer of 5 and 10 wt% NePCM samples can

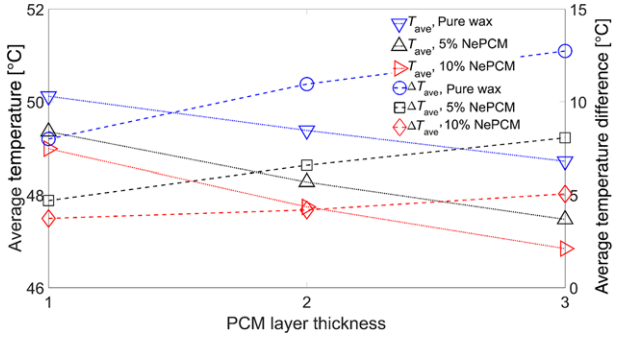

Figure 10. Variation of average temperature and average temperature difference in the module with PCM layer thickness.

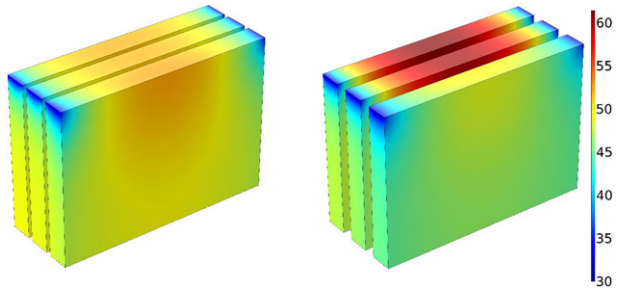

Figure 11. Temperature distribution in the module with 1 mm thick 10 wt% NePCM (left) and 3 mm thick pure wax at the end of the driving cycle (right).

maintain the batteries temperature about 1.2 and 1.9 °C lower compared to the pure wax.

Among the main factors influencing the performance and capacity fading of Li-ion batteries are the average and gradient of temperature. The time average of the batteries temperature difference is of interest because of multiple repetitions of the drive cycle in HEV which can be defined as follows:

$$\Delta T = \max \left[\frac{1}{t_{\text{cycle}}} \int_{t=0}^{t_{\text{cycle}}} \left(T_{\max(t),i} - T_{\text{ave}(t),i} \right) dt \right] \quad 0 < t < 1400\,\text{s} \tag{12}$$

where $i = 1, 2, 3$ represents each battery in the simulated module, and t_{cycle} is the driving cycle duration (1400 s).

Figure 10 shows the effects of PCM layer thickness on the batteries average temperature and average temperature difference. As mentioned before, the average temperature decreases with increasing thickness of all PCM samples studied. However, Figure 10 depicts that the average temperature difference slightly increases with PCM layer thickness in all cases. Increasing the thickness causes more heat accumulation in the PCM which forms higher temperature spots in the module. The results suggest that there is a trade-off between the average rise and uniformity of temperature that should be considered in the BTMS design.

Figure 11 shows the module temperature distribution at the end of the driving cycle in two limiting cases studied in this section, that is, 3 mm thick pure wax and 1 mm thick 10 wt% NePCM. In the pure wax system, the inner batteries temperature

Table 8. Melted fraction of the PCM at the end of the driving cycle.

PCM	Pure wax			5 wt% NePCM			10 wt% NePCM		
	1 mm	2 mm	3 mm	1 mm	2 mm	3 mm	1 mm	2 mm	3 mm
Melted fraction	78%	74%	71%	9%	14%	18%	0%	3%	4%

is obviously higher compared to the outer battery. A thick layer of pure paraffin with low thermal conductivity tends to store the batteries heat generated with no effective heat rejection to air, and therefore, fails to keep the battery temperature lower than its melting point. As shown in Figure 11, using a 1 mm layer of 10 wt% NePCM can successfully generate a moderate and relatively uniform temperature distribution in the module.

It has been shown that using Biot number to assess the thermal management efficiency of Li-ion battery modules may result in an error of 15% in total thermal energy.[11] This is mainly due to the highly non-homogeneous heat generation and thermal conductivity of the batteries. Therefore, in the present work, the effects of Biot number are not further investigated.

Table 8 shows the melted fraction of PCM under various design configurations. As a general trend, the melted fraction decreases with both PCM layer thickness and nanoparticles loading. A thicker layer of PCM provides more available sensible heat storage capacity that results in lower melting (latent heat storage). Furthermore, the thermal conductivity of the PCM enhances with the nanoparticle loading, which leads to more efficient heat rejection to the cooling air, and therefore, lower total melted fraction of the PCM. As mentioned before, the complete melting of PCM should be avoided because of the significantly lower thermal conductivity of liquid phase PCM. Hence, a thin layer of 10 wt% NePCM presents a more stable thermal management with a relatively uniform temperature distribution.

4.4.2. Effects of Air Inlet Temperature

In addition to the PCM layer thickness, another quantity of interest for assessing the performance of the BTMS is the air inlet temperature. Three values of air temperature namely 20, 30, and 40 °C are examined. In the simulations, the initial temperature of batteries is equal to the air inlet temperature which implies the application of air at ambient temperature.

Figure 12 shows the effects of air inlet temperature on the average batteries temperature rise using different PCM samples. A trend similar to the effect of the PCM layer thickness is observed. Higher air inlet temperatures increase the average temperature due to less heat rejection capacity from the batteries to the air. As can be seen from Figure 12, the average temperature is higher in the pure wax design compared to NePCM systems because of its lower thermal conductivity.

Table 9 shows the maximum temperature of batteries under various PCM samples and air temperatures. This table shows that the module thermal performance is a strong function of air temperature and utilizing 5 and 10 wt% mass fraction of nanoparticles can lower the maximum temperature by about 1.0 and 1.7 °C, respectively.

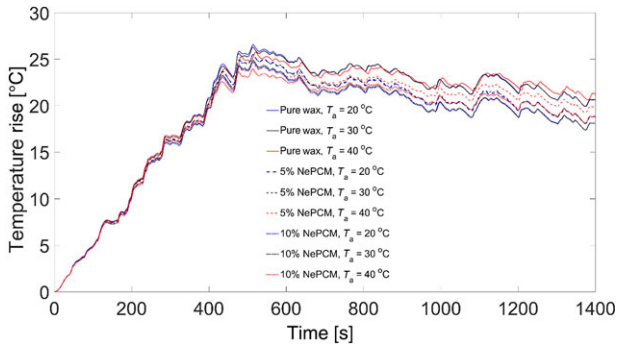

Figure 12. Variation of batteries average temperature under various PCM samples and air temperatures.

Table 9. Maximum temperature in the module at various air temperatures.

PCM sample	$T_a = 20$ °C	$T_a = 30$ °C	$T_a = 40$ °C
Pure wax	46.6	56.3	65.8
NePCM, 5 wt%	45.5	55.5	64.6
NePCM, 10 wt%	44.7	54.9	64.0

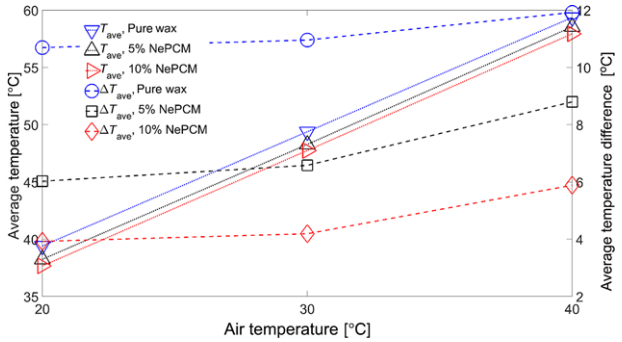

Figure 13. Variation of average temperature and average temperature difference in the module with air temperature.

Figure 13 shows the effects of air inlet temperature on the thermal behavior of the battery module. As depicted in this figure, the average temperature increases linearly with the air temperature. However, the average temperature difference increments faster after $T_a = 30$ °C, which shows the effects of the PCM layer on enhancing the temperature uniformity in the module at lower air temperatures. At $T_a = 40$ °C, the batteries average is close to the PCM sample's melting point (60 °C), which implies that a thin layer of melted PCM forms close to the batteries. As shown in Figure 4, the thermal conductivity of all PCM samples drops during the melting process, which represses the heat conduction from the batteries and leads to high temperature regions in the module. Therefore, only the solid and mushy phase PCM can absorb heat generation from the batteries surface and improve their temperature uniformity. This suggests that the operation and geometrical parameters should be selected with great care to keep the PCM at temperatures lower than the melting temperature.

Table 10 represents the melted fraction of PCM with various air temperatures and PCM samples. As this table suggests, the meted fraction does not significantly change with the air

Table 10. Melted fraction of the PCM at the end of the driving cycle.

PCM	Pure wax			5 wt% NePCM			10 wt% NePCM		
	$T_a = 20\,^{\circ}C$	$T_a = 30\,^{\circ}C$	$T_a = 40\,^{\circ}C$	$T_a = 20\,^{\circ}C$	$T_a = 30\,^{\circ}C$	$T_a = 40\,^{\circ}C$	$T_a = 20\,^{\circ}C$	$T_a = 30\,^{\circ}C$	$T_a = 40\,^{\circ}C$
Melted fraction	73%	73%	74%	14%	15%	15%	3%	3%	3%

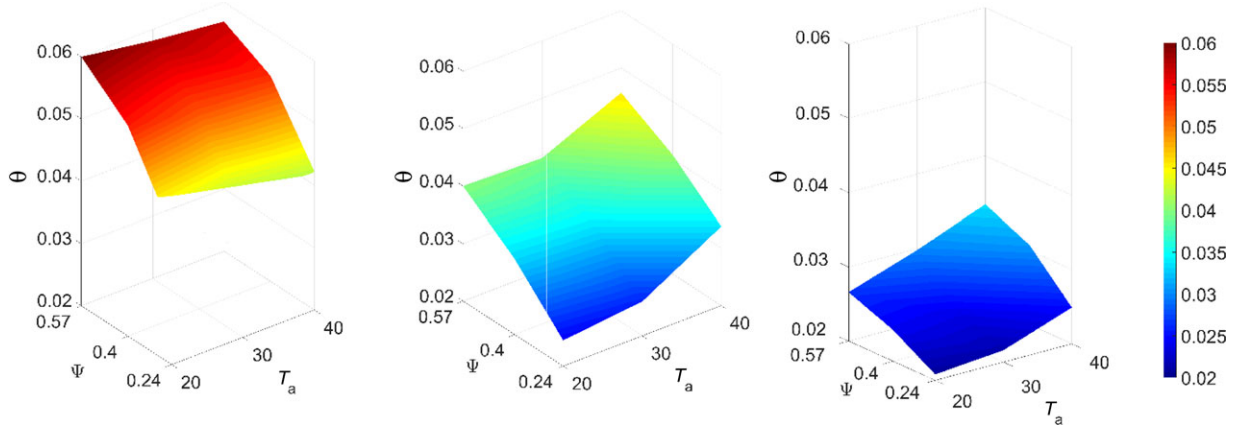

Figure 14. Dimensionless temperature difference (θ) in the module as a function of T_a and Ψ under pure wax (left), 5 wt% NePCM (center), and 10 wt% NePCM (right).

temperature. As mentioned in the previous section, the dominant heat resistance in the battery module is heat conduction, therefore, varying the air temperature does not affect the temperature distribution and the PCM melted fraction considerably.

In order to further investigate the effects of proposed BTMS design parameters on the module temperature distribution, two dimensionless parameters are defined as follows:

$$\theta = \max\left(\frac{T_{\max(t)} - T_{\text{ave}(t)}}{T_{\text{ave}(t)}}\right)_i, \quad i = 1, 2, 3 \quad 0 < t < 1400\,\text{s} \quad (13)$$

$$\psi = \frac{\text{Volume of the module}}{\text{Volume of batteries in the module}} - 1 \quad (14)$$

where θ represents the relative temperature non-uniformity caused by inadequate heat rejection form the batteries and Ψ indicates the module volume increase due to the utilization of the cooling system.

Figure 14 exhibits the effects of PCM layer thickness and air temperature on the dimensionless temperature difference θ. As shown in this figure, for all PCM samples, the temperature distribution is more sensitive to the thickness of the plates (Ψ) and the module temperature uniformity enhances with nanoparticles mass fraction due to higher thermal conductivity of NePCM samples compared to pure wax. This suggests that conduction in the BTMS is the dominant thermal resistance, and optimization attempts should mainly focus on enhancing conduction in the battery module. Additionally, this figure shows that a more compact and effective BTMS design can be achieved by using nano-enhanced PCM compared to pure wax.

As can be seen in Figure 14, when the air temperature increases the pure wax system shows a different trend compared to the NePCM samples. Higher values of air temperature decrease

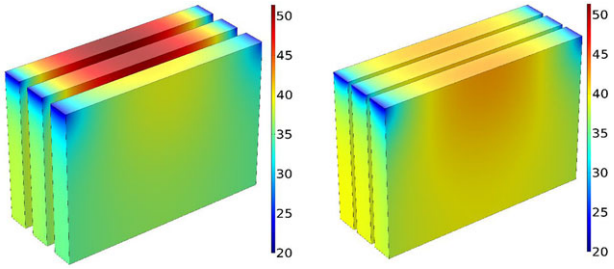

Figure 15. Temperature distribution in the module with 3 mm thick pure wax (left) and 1 mm thick 10 wt% NePCM (right) at the end of driving cycle.

the values of θ in the pure wax system while they increase θ in the NePCM cooling systems. As mentioned above, at elevated values of air temperature, a melted layer of the PCM sample forms close to the batteries surface. The high viscosity of NePCM (Figure 6) degrades the natural convection in the liquid phase materials and leads to a weak heat dissipation from the batteries. However, the natural convection heat transfer in the pure wax improves with temperature which results in lower values of θ at higher air temperatures.

The module temperature distribution at the end of the driving cycle is shown in **Figure 15**. This figure illustrates the results of the limiting cases corresponding to the conditions where the values of θ are maximum and minimum (worst vs best case of temperature uniformity). In both designs, the maximum temperature is shifted to the top center of batteries due to the presence of cooling channels at the sides of batteries. The maximum temperature location is slightly to the left because of higher heat generation in the batteries positive tab. **Table 11** compares the

Table 11. Average and maximum temperature of batteries under various BTMS designs.

Design	Battery 1 average/maximum temperature [°C]	Battery 2 average/maximum temperature [°C]	Battery 3 average/maximum temperature [°C]
Pure wax, $t = 3$ mm, $T_a = 20$ °C	35.8/40.7	39.5/50.6	40.6/51.2
10 wt% NePCM, $t = 1$ mm, $T_a = 20$ °C	38.8/42.7	39.0/42.0	39.3/42.0

average and maximum temperature of batteries in these designs. Although both designs can maintain the batteries temperature within the safe limits, the high temperature non-uniformities in pure wax system may result in capacity difference between the batteries and lower the lifespan of the module. However, the 10 wt% NePCM system is able to successfully maintain the temperature difference between batteries lower than 0.5 °C and the maximum temperature difference over a single battery is 3.9 °C (battery 1). Therefore, this design is a promising system to control the temperature of the batteries and keep the module temperature relatively uniform during the driving cycle.

5. Conclusions

A hybrid air-cooled active–passive thermal management system is developed to address the raising concerns regarding the potential failures of passive PCM-based thermal management systems. A fast simulation coupled electrochemical–thermal model is used to predict the thermal responses of Li-ion batteries during a standard driving cycle. The results show that the PCM layer makes the active control of air velocity and/or temperature unnecessary or complementary, and therefore, provides a simplified, compact, and low-cost design. The PCM can absorb batteries heat generation during the highly dynamic driving cycles and transfer the stored heat at a relatively constant temperature to the air flow. Furthermore, the presence of PCM enhances temperature uniformity over the batteries surface by absorbing more heat from the region close to the battery tabs.

The techniques used to enhance the thermal conductivity of the pure PCM, that is, utilizing graphite nanopowder and HOPG sheets, demonstrate promising capability to solve the problem of inherently low thermal conductivity of the organic PCM. A highly conductive PCM improves the heat transfer from the batteries to the cooling air and maintain the batteries temperature within the safe limits. Forced-air cooling has a critical role in thermal storage capacity recovery of the PCM. The lack of effective active cooling may result in heat accumulation and thermal runaway in the battery module.

The proposed strategy offers excellent temperature uniformity among the batteries in the module by using a constant air flow during the driving cycle. The results revealed that there is a trade-off between average temperature and temperature uniformity of batteries that can be achieved by selecting an appropriate thickness of PCM layer. Furthermore, it is experimentally shown that the thermal conductivity of pure wax and NePCM samples drop during the melting process, which may result in heat accumulation in the material. This suggests that the PCM should remain in the solid or mushy phase during the driving cycle to prevent temperature non-uniformities in the module. The proposed hybrid thermal management system demonstrates advantages such as simple structure, no need for complex coolant control, low operating and maintenance costs, and high efficiency compared to conventional cooling systems.

Acknowledgements

The lead author is most grateful to the Ontario Trillium Foundation for an Ontario Trillium Scholarship.

Nomenclature

Cp	specific heat [J kg^{-1} K^{-1}]
g	gravity acceleration vector [m s^{-2}]
h	convection heat transfer coefficient [W m^{-2} K^{-1}]
H	container height [m]
I	identity matrix
k	thermal conductivity [W m^{-1} K^{-1}]
L	latent heat [J kg^{-1}]
n	normal vector
p	static pressure [Pa]
q''	heat flux [W m^{-2}]
R	container radius [m]
t	time [s]
T	temperature [K]
$T\infty$	ambient temperature [K]
u	velocity vector [m s^{-1}]

Greek Letters

μ	dynamic viscosity [Pa s]
ρ	density [kg m^{-3}]
ϕ	mass fraction

Subscripts and Superscripts

a	air
ini	initial
max	maximum
np	nanoparticle

Conflict of Interest

The authors declare no conflict of interest.

Keywords

electrochemical–thermal battery modeling, hybrid electric vehicles, lithium-ion battery modules, nano-enhanced phase change materials, thermal management

Received: February 5, 2018
Revised: March 8, 2018
Published online: April 30, 2018

[1] T. M. Bandhauer, S. Garimella, T. F. Fuller, *J. Electrochem. Soc.* **2011**, *158*, R1.
[2] G. Karimi, X. Li, *Int. J. Energy Res.* **2013**, *37*, 13.
[3] W. Tong, K. Somasundaram, E. Birgersson, A. Mujumdar, C. Yap, *Int. J. Therm. Sci.* **2015**, *94*, 259.
[4] A. Alrashdan, A. T. Mayyas, S. Al-Hallaj, *J. Mater. Process. Technol.* **2010**, *210*, 174.
[5] S. Wilke, B. Schweitzer, S. Khateeb, S. Al-Hallaj, *J. Power Sources* **2017**, *340*, 51.
[6] M. Zolot, A. Pesaran, M. Mihalic, presented at *Proceedings of the Future Car Congress*, Arlington, Virginia, **2002**.
[7] L. Fan, J. Khodadadi, A. Pesaran, *J. Power Sources* **2013**, *238*, 301.
[8] R. Sabbah, R. Kizilel, J. Selman, S. Al-Hallaj, *J. Power Sources* **2008**, *182*, 630.
[9] Y. Liu, *J. Cent. South Univ.* **2015**, *22*, 3970.
[10] S. Mohammadian, Y. Zhang, *J. Power Sources* **2015**, *273*, 431.
[11] Q. Wang, Q., B. Jiang, *Renew. Sustain. Energy Rev.* **2016**, *64*, 106.
[12] Z. Rao, S. Wang, *Renew. Sustain. Energy Rev.* **2011**, *15*, 4554.
[13] Y. Huo, Z. Rao, *Energy Convers. Manag.* **2015**, *89*, 387.
[14] L. Jin, P. Lee, *Appl. Energy* **2014**, *113*, 1786.
[15] T. Zhang, C. Gao, *Appl. Therm. Eng.* **2015**, *88*, 398.
[16] S. Hallaj, J. Selman, *J. Electrochem. Soc.* **2000**, *147*, 3231.
[17] X. Duan, G. Naterer, *Int. J. Heat Mass Transf.* **2010**, *53*, 5176.
[18] N. Javani, I. Dincer, G. Naterer, *Int. J. Heat Mass Transf.* **2014**, *72*, 690.
[19] W. Li, Y. Tao, *J. Power Sources* **2014**, *255*, 9.
[20] R. Kizilel, A. Lateef, R. Sabbah, M. Farid, S. Al-Hallaj, *J. Power Sources* **2008**, *183*, 370.
[21] L. Liu, D. Su, Y. Tang, *Renew. Sustain. Energy Rev.* **2016**, *62*, 305.
[22] J. Khodadadi, L. Fan, H. Babaei, *Renew. Sustain. Energy Rev.* **2013**, *24*, 418.
[23] H. Fathabadi, *Energy* **2014**, *32*, 555.
[24] Z. Ling, F. Wang, *Appl. Energy* **2015**, *148*, 403.
[25] Y. Tang, Y. Liu, *J. Electrochem. Soc.* **2014**, *161*, E3021.
[26] C. Pals, J. Newman, *J. Electrochem. Soc.* **1995**, *142*, 3282.
[27] A. Eddahech, O. Briat, J. Vinassa, *Energy* **2013**, *61*, 432.
[28] N. Dhaidan, J. Khodadadi, T. Al-Hattab, S. Al-Mashat, *Int. J. Heat Mass Transf.* **2013**, *67*, 523.
[29] Y. Feng, H. Li, *Int. J. Heat Mass Transf.* **2015**, *81*, 415.
[30] L. Fan, Z. Zhu, Z. T. Yu, *Int. J. Heat Mass Transf.* **2014**, *79*, 94.
[31] A. Ghossein, M. Hossain, J. Khodadadi, *Int. J. Heat Mass Transf.* **2017**, *107*, 697.
[32] H. Care, S. Net, E. Marion, *Nat. Research Coun.* **2000**, *233*, 15.
[33] A. Santucci, A. Sorniotti, C. Lekakou, *J. Power Sources* **2014**, *258*, 395.
[34] K. Gokce, A. Ozdemir, *Int. J. Electrochem. Sci.* **2016**, *11*, 1228.

Powder Binders Used for the Manufacturing of Wind Turbine Rotor Blades. Part 1. Characterization of Resin-Binder Interaction and Preform Properties

Stefan Schmidt, Thorsten Mahrholz, Alexandra Kühn, Peter Wierach
German Aerospace Centre (DLR), Institute of Composite Structures and Adaptive Systems, Lilienthalplatz 7, Braunschweig, D-38108, Germany

Glass fiber reinforced plastics (GFRP) are the predominant materials used for wind turbine rotor blades. To manufacture blades in a vacuum-assisted resin infusion process (VARI), a binder is needed for fiber fixation and preform stability. Moreover, solubility and mechanical compatibility of the binder and the epoxy resin matrix are important parameters for processability and the mechanical properties of the composite. The present study therefore characterized and evaluated five chemically different binders with regard to their solubility in a rotor-blade-proven epoxy resin using microscopy, viscometry, and differential scanning calorimetry (DSC). The solubility tests enabled a binder-classification into critically soluble (KE-60, Epikote 05390), strongly soluble (Grilon MS), partially soluble (D 2433E), and nonsoluble (K-140) binder types. In subsequent mechanical and thermo-mechanical testing of resin-binder plates, the strongly soluble binder Grilon MS showed the best performance, followed by the nonsoluble binder K-140 and the partially soluble binder D 2433E. These results suggest that binders developing no interfaces within the resin should be preferred. Furthermore, interply adhesion for these three binders was investigated in a peeling test using fiber preforms. It was found that differences in peel strength might be controlled predominantly by different kinds of binder layer formations, but also to some extent by the different binder-fiber interaction (binder and fiber sizing correlation). Best performance was shown by D 2433E, followed by Grilon MS and K-140. All in all, the soluble binder Grilon MS exhibited the best results in mechanical testing of resin-binder plates and is therefore expected to also show the best mechanical performance in GFRP laminates. POLYM. COMPOS., 39:708–717, 2018. © 2016 Society of Plastics Engineers

Correspondence to: T. Mahrholz; e-mail: thorsten.mahrholz@dlr.de
Contract grant sponsor: German Federal Ministry for Economic Affairs and Energy; contract grant number: AZ0325601A/B/C/D.
DOI 10.1002/pc.23988
Published online in Wiley Online Library (wileyonlinelibrary.com).

INTRODUCTION

Manufacturing of wind turbine rotor blades is strongly driven by the use of low cost materials and production processes. The goal in the near future is to reduce production time through automated manufacturing procedures and by using more cost-efficient materials, in both cases taking into account the need for higher quality of produced rotor blades. A strong focus on rotor blade quality will particularly be necessary if rotor blade size increases. Currently, liquid composite molding processes such as vacuum-assisted resin transfer molding (VARTM) have been recognized as successful manufacturing methods in the rotor blade industry. This technology usually requires pre-cut fiber semi-finished fabrics which are manually laid down, stacked, aligned, and bound together by binders in the bottom and/or top half of a blade-shaped mold forming the corresponding preform. In general, the binders used for preforming processes in the manufacturing of rotor blades have to meet typical requirements: development of strong interply adhesion forces (high peel strength) to prevent any slipping of the fiber semi-finished product at vertical tooling surfaces (e.g., blade root); prevention of unwanted wrinkling of fabric layers, as undulation reduces mechanical performance of the composite part; minimal effect on the required fiber volume ratio in the final GFRP; easy handling and processing; no wash-out effect during resin infusion process, preventing an increase in resin viscosity; binder and resin must be adjusted with respect to their chemical composition in order to achieve the highest possible mechanical compatibility.

Nowadays, binder systems used in industrial rotor blade manufacturing are predominantly applied manually in the form of spray adhesives (e.g., SW7808, Co. 3M), hot-melt adhesives, adhesive tapes (e.g., SaerfixEP, Co. SAERTEX) or glass fabric adhesive grid tapes. These typical binder systems are generally characterized by high interply adhesion forces and mostly based on low melting thermoplastic materials (polyester, polyamide) or thermosetting resins (epoxy, cyanoacrylate) that vary in their solubility and reactivity with

the infusion resin matrix. Interply adhesion forces, measured by peeling tests, depend on binder loading, processing parameters and binder type. In general, peel strength rises with increasing binder loading until the surface of the fabric is fully covered [1]. A further increase in binder loading does not enhance binder-fiber interaction. At higher binder activation temperatures the viscosity of the binder can be lowered, allowing the binder to wet and infiltrate the fiber tows more easily and leading to further enhancement of binder-fiber interaction [2]. However, if too much of the binder mass infiltrates the fiber tows, less adhesion is achieved in the interply region, leading to lower peel strengths. A similar influence may be observed using different binder particle sizes; small particles can infiltrate the fiber tows more easily than larger particles. It is evident that increasing particle size from 40 μm to 1,000 μm significantly increases peel strength [3]. The chemical compatibility of fiber sizing and binder also results in different peel strengths. Brody and Gillespie [4] observed a much higher peel strength using a reactive epoxy binder rather than a thermoplastic polyester binder. Better binder- fiber interaction was expected due to the epoxy-compatible silane fiber sizing.

Both springback and bending stiffness are important parameters for preform stability. Normally, preform binders reduce springback and raise bending stiffness, especially if the binder is located within the fiber layers, because this intralayer coverage stiffens the fiber tows [3, 5]. Moreover, it is to be expected that the higher the tensile modulus of the binder, the more effective the reduction in springback. If the binder is applied in line or point patterns instead of full surface coverage, bending stiffness is reduced [2]. For complex shaped preforms, low bending stiffness may be essential to maintaining drapeability [6].

In resin infiltration processes, the binder may act as a barrier layer and decrease permeability of the preform, especially if the binder is located between, instead of inside, the fiber layers [5, 7]. Furthermore, it is known that soluble binders increase resin viscosity, thus hindering mold filling (decreased permeability) and resulting in unequal binder migration with varying local concentrations [8]. It can be assumed that reducing injection temperature and duration of contact between the flowing resin and the fixed binder lowers the risk of dissolving. Depending on the binder location (interlayer vs. intralayer coverage), pores may be formed in the interply region or inside the fiber tows, respectively, because the binder acts as a barrier [9].

Moreover, binders that are primarily located in the interply region may increase preform thickness, leading to a reduced fiber volume ratio of the composite [2, 10].

Manual application is disadvantageous for all binder systems, resulting in uneven and inhomogeneous distribution and local overloading of binder onto the fabric surface. Consequently, the mechanical and thermal properties across the preform and the corresponding composite part are affected differently. Moreover, for composites it is known that the higher the binder concentration, the lower the mechanical strength and glass transition temperature [1, 2, 11]. On the other hand, toughness and CAI performance increase [4, 11, 12]. These observations underline the need for compatible resin and binder systems to achieve optimal mechanical performance in rotor blade composites. To investigate resin-binder compatibility, solubility tests, and mechanical characterization of resin-binder plates (without reinforcing fibers) must be performed. Brody and Gillespie [13] observed for a polyester binder in a vinyl ester resin that initial viscosity, T_g, tensile strength and tensile strain at break of resin-binder mixtures rose with increasing binder content. A similar increase in tensile strength and tensile strain at break was observed with intensified binder dissolution, achieved by dissolution time. Cherif et al. [2] combined an epoxy-amine resin with several binders of different chemical types (e.g. epoxy, phenoxy, styrene-acrylic ester, unsaturated polyester). All binders raised the initial resin viscosity by about 50% − 150%. Furthermore, an extreme rise in viscosity was observed with increasing binder content. In tensile testing of resin-binder plates, only one binder decreased mechanical performance. However, the viscosity increase of this binder was comparable to the other binders. Tanoğlu and Seyhan [14] modified an unsaturated polyester matrix with a thermoplastic polyester binder. Viscosity was raised with increasing binder content and partial solubility was confirmed by microscopy. However, the compressive strength of the resin-binder mixture was comparable to the strength of the neat resin.

In this article, five different binders — thermoplastics and thermosets — are investigated with respect to their application in rotor blade manufacturing. Qualified binders have to meet special processing and mechanical parameters, as mentioned. Therefore, binder type and loading for a rotor-blade-proven epoxy resin are varied. The corresponding mixtures are characterized in terms of solubility, viscosity, mechanical, and thermal properties. Furthermore, the quality of fiber preforms is investigated by measuring interply adhesion with a peeling test and by determining the formation of binder layers via microscopy. The binders are evaluated taking these parameters into consideration. Moreover, relationships between binder type and loading with respect to their mechanical performance are derived. The long-term objective of this investigation is to reveal that solubility tests and mechanical testing of resin-binder plates can be used as simple screeing methods for binder preselection. It is assumed that the results can be directly linked to the mechanical performance of binder-modified GFRP.

MATERIALS AND METHODS

Materials

In this study, five commercially available powder binders of differing chemical composition were selected and evaluated in terms of resin-binder interaction and preform properties. The study predominantly examined nonreactive thermoplastics such as polyhydroxyether/phenoxy (Grilon MS), polyester (KE-60), co-polyamide (K-140), and co-polyester (D 2433E)

TABLE 1. Overview of used powder binders.

Binder type	Supplier	Chemical type	Particle size[a] X_{50} (μm)	Melting range (melting peak)[b] T_m (°C)
Grilon MS	EMS	Polyhydroxyether	59.5	Amorphous
KE-60	EMS	Polyester (PES)	60.2	33 – 62 (58)
K-140	EMS	Co-polyamide (Co-PA)	52.0	104 – 155 (129)
D 2433E	EMS	Co-polyester (Co-PES)	57.0	87 – 133 (107)
Epikote 05390	Momentive	Epoxide (EP)	59.0	52 – 66 (61)

[a]Particle sizes were determined by laser diffraction technique and based on averaged mass values (Q3).
[b]Melting range and corresponding peak temperature (in brackets) were determined by DSC.

provided by EMS-Chemie AG (Switzerland), but also focused on an epoxy binder (Epikote 05390 from the company Momentive) which can be described as a reactive thermoset resin without hardener component. A detailed overview of the used binders and the corresponding physical and thermal parameters is given in Table 1. Particle size and melting range were determined by laser diffraction (HELOS, Sympatec) and differential scanning calorimetry (DSC, Type DSC 822^e, Mettler Toledo), respectively. At this point the binders Grilon MS and Epikote 05390 might be described as potentially soluble since they contain hydroxyl and epoxy groups, respectively. Details on the definite chemical structures of the binders were not provided by the suppliers. The epoxy resin Airstone 880E with the corresponding amine hardener Airstone 886H was used as the polymer matrix. Both components were provided by Dow Chemical and approved by Germanischer Lloyd (DNV GL) for the manufacturing of wind turbine blades. The mixing ratio of resin to hardener was 100: 31. Mixing was carried out at room temperature, followed by a short degassing step. The curing cycle was set to 80°C for 5 h. To characterize the adhesive properties of the binders, different preform samples were prepared, varying in binder type and content. A unidirectional E-glass fabric (U-E-1,200 g/m^2−1,300 mm, Saertex) with a weft content of 5 wt% was used as fiber semi-fabric.

Solubility Tests

Resin-binder mixtures with a binder content of 3 wt% were prepared and tested for binder solubility to derive a correlation of solubility and mechanical performance. Resin, hardener, and binder were mixed with a mechanical stirrer (RZR 2102 control, Heidolph Instruments) at 1,000 rpm. The mixture was degassed using a magnetic stirrer (MR Hei-End, Heidolph Instruments) at 400 rpm for 10 min in a desiccator evacuated below 1 mbar with a vacuum pump.

To examine binder particle morphology, the mixtures were placed between two microscope slides. From each mixture, one set of samples was cured at RT for 24 h and the other set at 80°C for 5 h. These samples were examined with a digital microscope (VHX-1000, Keyence). Binders are classified as soluble if the particles disappear and no residue can be distinguished. Criteria for partially soluble binders are shrunk particles, rounded edges or differently shaped residue. If no morphological changes occur, the binder is regarded as nonsoluble.

Additionally, the effect of the binder on resin viscosity was determined using a rotational viscometer (Gemini 150, Malvern Instruments) in pate-pate mode (plate diameter: 40 mm). Tests were performed isothermally at 40°C (lowest constant temperature possible) with a shear rate of 40 Hz. If the binder is dissolved within the resin, an increase in viscosity can be observed due to intensified molecular friction.

Finally, DSC tests were performed to underline the state of binder solubility using the aforementioned resin mixtures with 3 wt% binder, cured at 80°C for 5 h. Compared to the neat resin, additional endothermic peaks in the DSC curve illustrate the existence of a separate binder phase. With regard to this information, three cases have to be distinguished. If the binder is dissolved in the matrix, its melting enthalpy peak is expected to disappear, whereas the enthalpy of a nonsoluble binder remains unchanged in the DSC curve. If the binder is dissolved partially, the peak will be distinguishable but reduced in its specific enthalpy. A DSC 822^e (Mettler Toledo) was used and the temperature program set from 40°C to 160°C with a heat rate of 10°C/min.

Preparation and Characterization of Resin-Binder Plates

For further evaluation of resin-binder interactions, resin-binder plates were manufactured and characterized in mechanical and thermo-mechanical tests. The binders KE-60 and Epikote 05390 were discarded. The reasons are discussed in Section "results and discussion / solubility tests".

Resin and binder were mixed and degassed as described in the experimental part. Previous tests in plate molding showed binder migration, and consequently inhomogeneous distribution, due to density differences. To prevent this phenomenon, the mixture was heated at 40°C to raise its viscosity (no or low state of pre-gelation), followed by an additional mixing step. After plate molding, a curing temperature of 80°C was applied for 5 h. Plates with a binder content of 3, 7, and 11 wt% were manufactured. This corresponds to binder contents of 1, 2, and 3 wt% in GFRP composites showing the typical fiber volume ratios of 55% used in rotor blade manufacturing. Test samples were prepared using a milling machine (PASO Präzisionsmaschinenbau).

Tensile tests in accordance with the German industry standard DIN EN ISO 527-2 were performed using the

testing machine Zwick 1476 (Zwick/Roell). A biaxial extensometer (MTS Systems Corporation) was used to detect strain. Crosshead speed was set to 2 mm/min. For thermomechanical characterization, a dynamic mechanical thermal analysis (DMTA) was performed (DMA/SDTA861^e, Mettler Toledo). The temperature program was set from 0 to 160°C with a heat rate of 3°C/min. Samples with dimensions of 50 × 5 × 2.5 mm were loaded in a three-point-bending test. The load was set to 0.7 N and the frequency to 1 Hz. The onset temperature at the drop of the storage modulus and the glass transition temperature T_g (peak temperature of tan δ) were determined.

Preform Manufacturing and Testing

To evaluate the degree of binder layer formation and the interply adhesion properties of the different binders, two-layered fiber preforms with selected binders (Grilon MS, K-140 and D 2433E) were prepared.

In general, the binder was sprinkled onto the lower glass fabric surface using a sieve with a mesh size of 130 µm (F 4,000, METEX-Meschenmoser), applying surface loading of 24, 48, and 72 g/m^2. This corresponds to binder contents of 1, 2, and 3 wt% in GFRP composites showing the typical fiber volume ratios of 55% used in rotor blade manufacturing. The upper glass fabric was reversely placed on the lower fabric. The binder was thus located between the warp threads of the two fabrics. To activate the binder, the preforms were compacted using a vacuum bag and placed in an oven for one hour under constant evacuation. Evacuation was continued until the preforms cooled down below the binder melting temperature. Binder activation temperature was set to 190°C, 180°C, and 150°C for Grilon MS, K-140 and D 2433E, respectively. These temperatures are more than 20°C above the measured melting ranges (see Table 1). For the binder Grilon MS, which showed no melting range due to its amorphous structure, the temperature was determined at which the binder showed comparable consistency to the other binders.

Binder layer formation was investigated by microscopy. To this end, small samples of the cut prefoms were embedded within the epoxy resin EpoFix (Struers). To enhance contrast between binder and resin, the resin was modified with a dye (EpoDye, Struers). Infiltration of the embedding resin was supported by evacuation (≈100 mbar). Samples were polished using a Planpol 2/Pedemax 2 (Struers) and examined using a VHX-1000 microscope (Keyence).

To characterize adhesion properties, a T-peeling test in accordance with the test standard DIN EN ISO 11339 was performed. Strips with a width of 25 mm and a length of 340 mm were cut from the fiber preforms and clamped into the testing machine (Zwick Z005, Zwick/Roell). Crosshead speed was set to 50 mm/min. Mean peel strength (force divided by sample width) was calculated over a peeled sample length of 115 mm (230 mm crosshead distance); regions close to the edges of the preform were not taken into account.

RESULTS AND DISCUSSION

Solubility Test

Binder solubility was determined and evaluated using microscopy, viscometry, and DSC techniques. The results for the investigated binders are illustrated separately and compiled at the end of this section to derive conclusions.

Micrographs of all resin-binder mixtures after curing at RT and 80°C are shown in Fig. 1. After RT curing, no morphological changes in the binder particles can be found for samples modified with KE-60, K-140, and D 2433E. The number of Grilon MS particles however is reduced, the remaining particles are shrunk and their edges are rounded, indicating a high level of partial solubility. Particles of Epikote 05390 are not visible at all. After 80°C curing, the only binder that shows no morphological changes is K-140. No particles of Grilon MS, KE-60 or Epikote 05390 are distinguishable. The binder D 2433E shows drop-shaped residue and streaks instead of sharp-edged particles. Since curing occurred far below the melting range of the binder, these morphological changes can be attributed to solubility effects.

The isothermal viscosity curves of the neat resin and resin-binder mixtures are illustrated in Fig. 2. Sample code, initial viscosity and pot life (here empirically defined time until mixture reaches a viscosity of 500 m Pas) of all mixtures are listed in Table 2 together with the mechanical results. In general, all binders raise the initial viscosity and reduce the pot life of the resin. Depending on the type of binder the observed initial viscosity changes from slight ($\Delta\eta_{(D2433)}$: +7%) to extreme values ($\Delta\eta_{(KE\text{-}60)}$: +282%) compared to the neat resin. However, part of the increase in viscosity with KE-60 can be attributed to the melting of the binder. Viscosity measurements were performed at 40°C, which is below the melting peak but already in the melting range of this binder (see Table 1). Comparable effects have been observed by Cherif et al. [2] studying the influences of thermoplastic binders on epoxy resin viscosity. According to this study, binder contents of 5 wt% yielded an increase in initial viscosity of about 50% − 150%. In general, it must be noted that the measured increase in viscosity will be less distinct during resin infusion of the preform in the tooling. This is because after activation the binder forms a layered structure showing reduced specific surface area, resulting in smaller solubility effects. In contrast, in this study the binders were dispersed in the resin as particles, inducing a much higher specific surface area and exhibiting more interaction with the resin.

To underline the observed solubility results, additional representative DSC curves of selected resin-binder mixtures (3 wt% binder) were measured and are illustrated in Fig. 3. The melting peak of the binder K-140 can be clearly distinguished from the glass transition range of the resin. Related to the binder mass in the sample, this peak shows the same specific enthalpy as the neat binder. Furthermore, the T_g value does not change in comparison to the neat resin underlining the

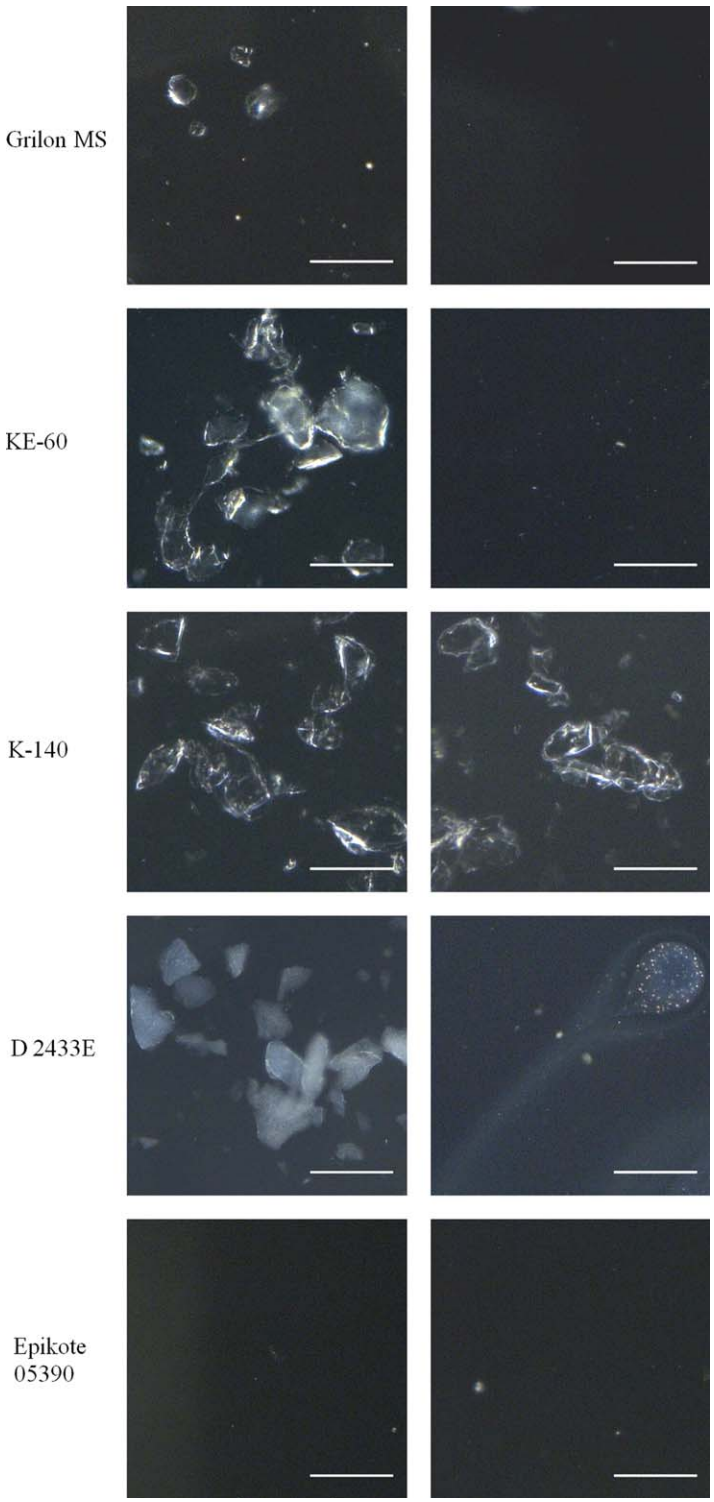

FIG. 1. Micrographs of resin-binder mixtures (binder content 3 wt%) cured at RT (left) and 80°C (right). Scale bar: 100 μm. [Color figure can be viewed at wileyonlinelibrary.com]

coexistence of two separated and unchanged phases. The binder was therefore not dissolved within the resin. In contrast, no endothermic peaks were observed for Grilon MS, KE-60 and Epikote 05390 (the last two binders are not illustrated in Fig. 3). These results suggest that the binders were completely dissolved. The specific enthalpy of the binder D 2433E was reduced by about 50% in the mixture, indicating partial solubility (for the purpose of clarity, the result is not illustrated in Fig. 3). Interestingly, T_g values of the investigated resin-binder mixtures and the neat resin are nearly identical independent of the degree of binder solubility. Especially in the case of soluble and partially soluble binders the slight effect on T_g is

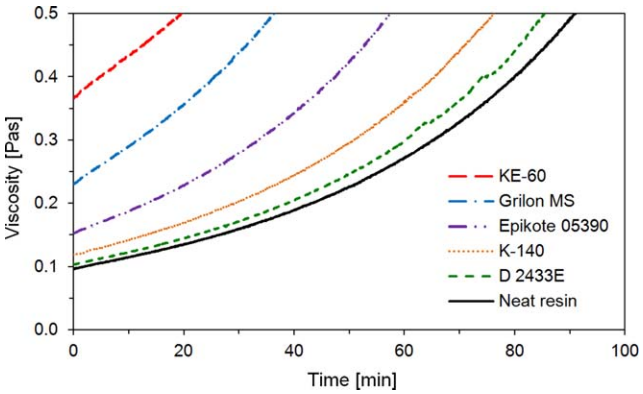

FIG. 2. Isothermal viscosity curves at 40°C of the neat resin and resin-binder mixtures (binder content 3 wt%) as a function of time. [Color figure can be viewed at wileyonlinelibrary.com]

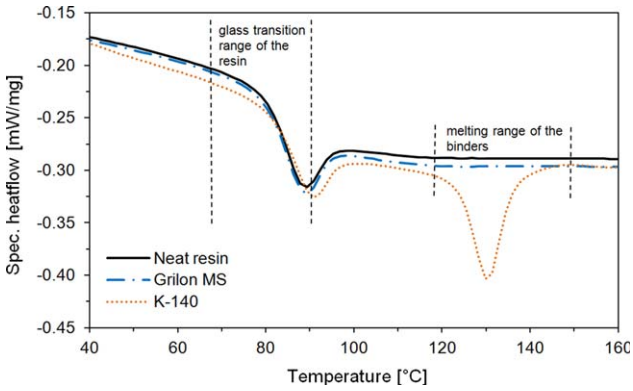

FIG. 3. DSC curves of the selected resin-binder mixtures with 3 wt% binder content. [Color figure can be viewed at wileyonlinelibrary.com]

surprising and might be attributed to the small binder content of 3 wt% used here.

A complete overview of the solubility test results is summarized and evaluated in Table 3. According to these results, all tests confirm a strong solubility of Grilon MS. The number of binder particles is reduced after RT curing, and no particles can be distinguished after curing at 80°C. This result is underlined by the strong increase in resin viscosity and the absence of endothermic peaks for the binder in the DSC curve. The strong solubility of the binder Grilon MS can be attributed to its hydroxyl groups showing good compatibility with the used epoxy resin (similar wettability properties). Furthermore, these functional groups may also enable chemical side reactions with the epoxy groups of resin. Similar testing results were obtained with the binder KE-60. Although particles can be clearly distinguished after RT curing, the increase in viscosity is more distinctive. Epikote 05390 shows similar phenomena to Grilon MS; its solubility is however greater since no particles can be observed after RT curing. This strong interaction can be explained by the good chemical compatibility of the epoxy binder and the epoxy resin as already mentioned above. In contrast to these soluble binders, no morphological changes can be observed in the K-140 particles after RT and 80°C curing, the increase in viscosity is only slight and the melting enthalpy of the binder can be found unreduced in the DSC curve of the mixture. The binder can therefore be classified as nonsoluble. D 2433E shows different behavior. After the 80°C curing, streaks instead of particles can be seen. Although no influence on resin viscosity is measured, a reduction in melting enthalpy is noted. The binder can therefore be classified as partially soluble.

In conclusion, two binders fail to meet the requirements of processing as previously stated. KE-60 yields an extreme rise in resin viscosity which may cause manufacturing problems. Furthermore, Epikote 05390 shows complete solubility at RT, which might result in wash-out effects and thus increased resin viscosity during the injection process. Both

TABLE 2. Overview of the prepared resin-binder systems (if not stated otherwise, standard deviations are below 5%).

			Viscosity at 40°C		Tensile test			DMTA[b]	
Sample code	Binder type	Binder content (wt%)	Start viscosity η (m Pas)	Pot life[a] t (min)	σ_t (MPa)	E_t (GPa)	ε_t (%)	T_{Onset} (°C)	T_g (°C)
Ref	—	—	96	90	60.3	3.00	7.02 ± 0.80	79.8	96.3
Phe-3	Grilon MS	3	230	36	63.4	2.93	5.94	74.6	91.2
Phe-7	Grilon MS	7	—	—	64.2	2.93	5.97	74.7	95.4
Phe-11	Grilon MS	11	—	—	64.4	2.91	6.14	74.2	94.2
KE60-3	KE-60	3	367	19	-	-	-	-	-
K140-3	K-140	3	118	76	59.9	2.82	6.31	72.9	93.0
K140-7	K-140	7	—	—	57.8	2.68	5.63	80.0	101.0
K140-11	K-140	11	—	—	54.7	2.56	4.79	71.2	91.3
2433-3	D 2433E	3	103	85	58.9	2.82	4.57	69.7	91.1
2433-7	D 2433E	7	—	—	54.8	2.62	5.08	69.6	91.8
2433-11	D 2433E	11	—	—	50.2	2.45	5.29	69.5	90.6
Epi-3	Epikote 05390	3	152	57	—	—	—	—	—

[a]All viscosity values were measured at 40°C. Pot life is defined as the time after the mixture reaches a viscosity of 500 m Pas.
[b]The dynamic mechanical thermal analysis (DMTA) was used to determine the onset temperature at the drop of the storage modulus and the glass transition temperature T_g (peak temperature of tan δ).

TABLE 3. Summary and conclusion of the binder solubility tests.

Binder type	Binder morphology after RT curing	Binder morphology after 80°C curing	Raise of resin viscosity	Binder enthalpy within resin	Conclusion
Grilon MS	Dissolved incompletely	Dissolved	Strong	No peak distinguishable	Strongly soluble
KE-60	Unchanged	Dissolved	Extreme	No peak distinguishable	Critically soluble
K-140	Unchanged	Unchanged	Slight	No reduction in peak enthalpy	Nonsoluble
D 2433E	Unchanged	Streaks	None	Peak enthalpy reduced about 50%	Partially soluble
Epikote 05390	Dissolved	Dissolved	Moderate	No peak distinguishable	Critically soluble

binders were therefore discarded for the ongoing evaluation. Consequently, the following mechanical testing focused on the strongly soluble binder Grilon MS, the nonsoluble binder K-140 and the partially soluble binder D 2433E classified in terms of the curing conditions used here.

Mechanical Characterization of Resin-Binder Plates

To observe resin-binder interactions under mechanical and thermal stress, a tensile test and a DMTA were performed on resin-binder plates. Results of these tests are summarized in Table 2. Tensile strength and tensile modulus are illustrated as a function of binder content in Fig. 4. The tensile strength of the resin-binder plates containing Grilon MS shows no dependency on binder content (≈ 64 MPa) and is slightly higher than the tensile strength of the reference (60.3 MPa). This matches the expectations since Grilon MS is completely dissolved or chemically bonded within the matrix, thereby forming a homogeneous material. A linear drop in tensile strength with increasing binder content (3, 7, and 11 wt%) is found with the binders K-140 (59.9 to 57.8 to 54.7 MPa) and D 2433E (58.9 to 54.8 to 50.2 MPa). This drop in tensile strength can be attributed to the nondissolved thermoplastic phases that form weak spots in the material. It is noteworthy that the partially soluble binder D 2433E shows a poorer performance than the nonsoluble binder K-140. A drop in resin tensile strength due to a thermoplastic binder was also noted by Cherif et al. [2], whereas different phenoxy and epoxy binders did not show any such effect. For the tensile modulus, all resin-binder systems show similar linear trends with increasing binder content (3, 7, and 11 wt%). While Grilon MS shows no changes (≈2.93 GPa), a linear drop is found in K-140 (2.82 to 2.68 to 2.56 GPa) and D 2433E (2.82 to 2.62 to 2.45 GPa). This drop is caused by the thermoplastic phases, which are expected to exhibit a lower tensile modulus than the epoxy resin. From these results it could be assumed that the mechanical performance of the resin matrix is also controlled by the degree of development of resin-binder interfaces. Especially the small differences between partially soluble and nonsoluble binders underline that any presence of interfaces strongly affects mechanical performance.

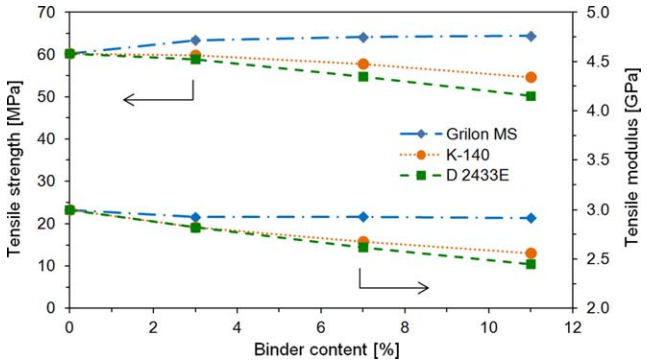

FIG. 4. Tensile strength and tensile modulus of resin-binder plates as a function of binder content and type. Standard deviations are illustrated but covered by the symbols. [Color figure can be viewed at wileyonlinelibrary.com]

Furthermore, the onset temperature and T_g (peak temperature of tan δ) are also influenced by the binders. Regardless of binder content, the onset temperature of the reference (79.8°C) is reduced to ≈ 74.5°C for Grilon MS, to ≈ 72°C for K-140 and to ≈ 69.6°C for D 2433E. However, unexpectedly the onset temperature of K140-7 is about 8°C higher compared to the onset temperatures of K140-3 and K140-11. This is treated as an outlier. Values of T_g are about 20°C higher than the onset temperature values and show the same trends described above.

Preform Properties

Following the mechanical characterization of resin-binder plates, preforms were prepared and investigated in micrographs and peeling tests, finding a correlation between the type of binder layer formation and the corresponding interply adhesion.

Micrographs of bindered preforms are shown in Fig. 5. The binder layer of Grilon MS exhibits gaps at all binder loadings. An increase in binder loading only enlarges the binder aggregations. In contrast, the binder layer of K-140 shows gaps at the lowest binder loading (24 g/m^2) but no gaps at higher binder loadings. The binder layer of D 2433E is nearly gapless at the lowest binder loading, and higher binder loadings only increase layer thickness. It has to be noted that for all binders the increase of binder loading from 48 to 72 g/m^2 results in a slight rise of interlayer thickness. The reason is that the higher the binder loading the more binder is displaced into the gaps

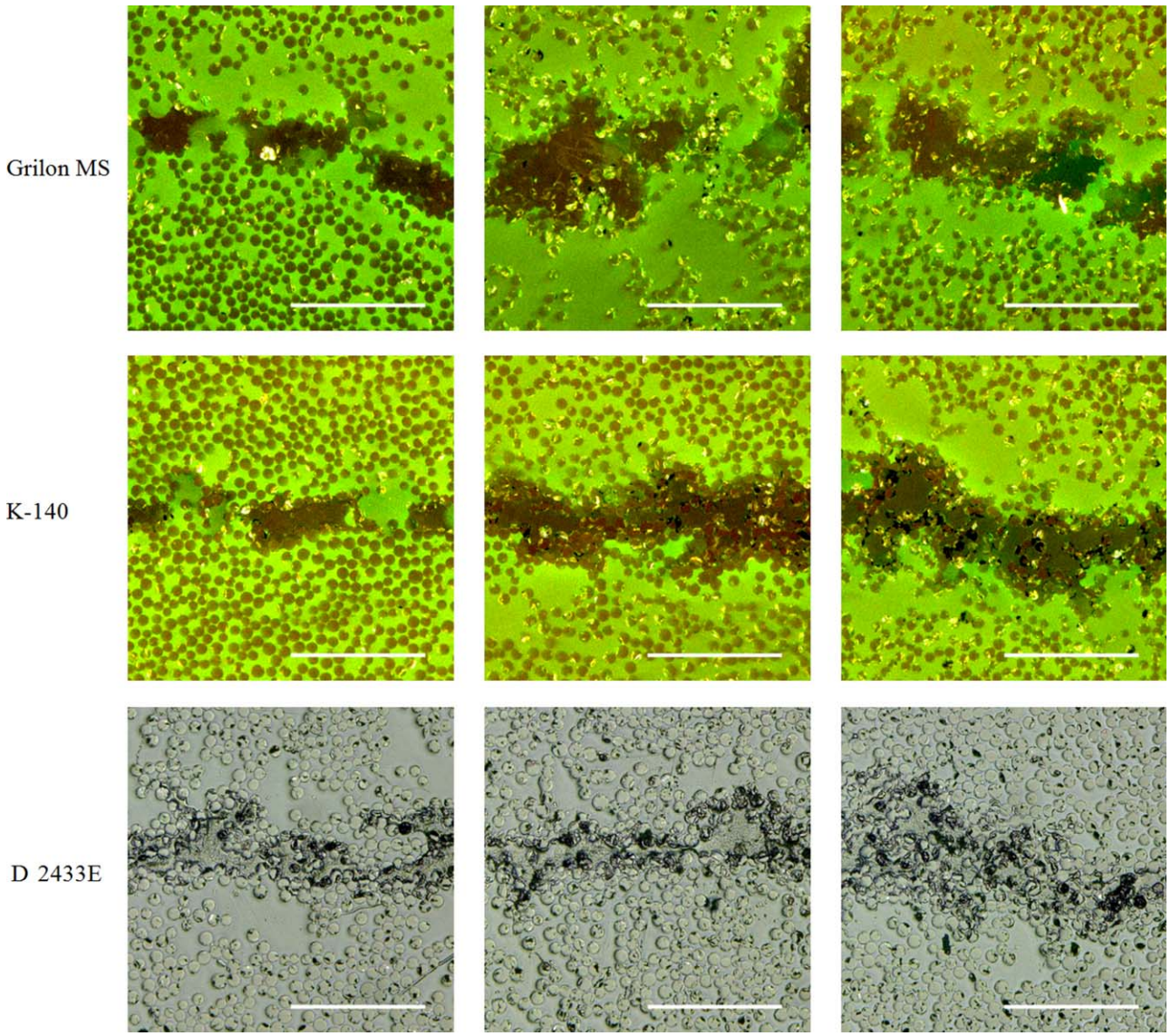

FIG. 5. Micrographs of bindered fiber preforms with a binder loading of 24 g/m^2 (left), 48 g/m^2 (middle), and 72 g/m^2 (right). Scale bar: 200 μm. Pictures of D 2433E were done at different microscope settings for better visibility. [Color figure can be viewed at wileyonlinelibrary.com]

between the rovings of the fiber layers during binder activation (regions not shown in Fig. 5). Regardless of binder type and loading, the binder does not infiltrate the fiber layers deeply in any of the preform samples. Consequently the binders are predominantly located in the interlayer (see Fig. 5).

During the peeling test, all samples showed stick/slip behavior as described in previous studies [2, 4, 15]. The failure pattern was the same for all binders (see Fig. 6). Cohesive failure occurred in the first 20 mm peeled sample length, since binder residues could be found on both split fiber layers (Fig. 6A). After about 20 mm the binder together with the knitting yarn and the weft threads of the lower fabric were detached (Fig. 6C), leaving only the warp rovings without binder residue (Fig. 6B). The measured peel strengths are shown in Fig. 7. Considering the standard deviations, the peel strength of the binder D 2433E exhibits no dependency on binder loading (≈ 11 N/cm). This can be explained by the micrographs presented in Fig. 5. Even the lowest surface loading of 24 g/m^2 yields a gapless binder layer. Therefore, an increase in binder loading increases interlayer thickness but does not enhance binder-fiber interaction (comparable surface of contact). Peel strength does not increase. The binder K-140 shows the lowest peel strength (4.8 N/cm) at the lowest binder loading (gaps are present in the binder layer), whereas the higher peel strength (≈ 7 N/cm) is not increased from 48 g/m^2 to 72 g/m^2 binder loading. The reason is that in both sets of samples no gaps are present in the binder layer and a levelling effect can be expected. Interestingly, the binder Grilon MS exhibits the highest peel strength at the lowest binder loading (10.5 N/cm in

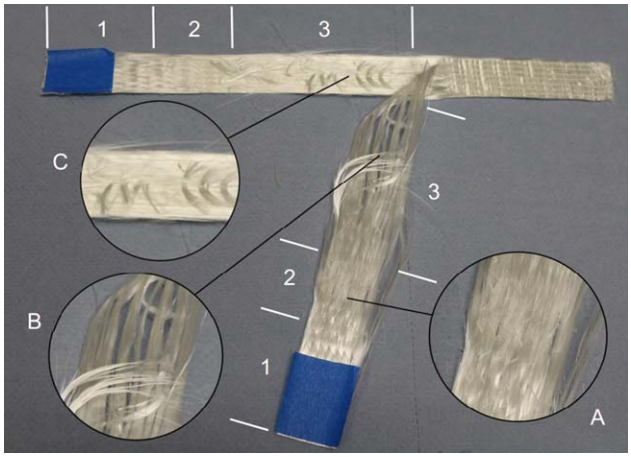

FIG. 6. General failure pattern of preform samples after T-peeling test. 1, Fixation region; 2, crack initiation region; 3, peel region. In Region 2 failure occurred cohesively (A) while in region 3 binder were detached from the lower fabric (B). The blue tape was used to facilitate the handling and fixation of the sample within the clamps. [Color figure can be viewed at wileyonlinelibrary.com]

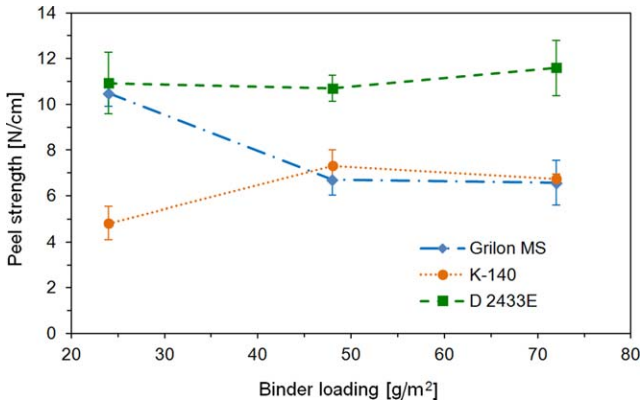

FIG. 7. Peel strength of bindered fiber preforms as a function of binder loading (24, 48, and 72 g/m^2) and type. [Color figure can be viewed at wileyonlinelibrary.com]

contrast to ≈ 6.6 N/cm at higher binder loadings), although gaps can be found regardless of binder loading. Additional tests will have to be carried out to explain this observation.

The difference in peel strength of the investigated binders must be attributed to the different chemical interactions between binder type and fiber sizing. However, details on the chemical structure of the binders and the fiber sizing are unknown. The measured peel strengths of 5 − 12 N/cm are in good accordance with literature values [2, 3]. However, higher values of up to 25 N/cm using reactive epoxy binders are also reported [4].

CONCLUSIONS

Preforming binders have to be chosen carefully to meet the requirements of the preform process (high interply adhesion) and the resin infusion process (low solubility within resin and slight effect on viscosity) as well as to reach the needed overall mechanical properties of GFRP used for wind turbine rotor blades. This study investigated five binders with different chemical compositions and therefore different resin solubilities. The mixtures are characterized in terms of solubility, viscosity, mechanical, and thermal properties.

Combining various analytical devices such as microscopy, viscometry, and DSC enables a detailed evaluation of solubility. Based on this procedure, the two binders KE-60 and Epikote 05390 can be considered critically soluble in this investigation. Extreme increases in viscosity and complete solubility at room temperature were observed, respectively. The three remaining binders were classified as strongly soluble (Grilon MS), partially soluble (D 2433E) and nonsoluble (K-140). Furthermore, the best mechanical performance of resin-binder plates is achieved with the strongly soluble phenoxy-binder Grilon MS. In this case, idenpendent of binder content, the tensile strength, modulus and fracture strain do not differ from the reference and the drop in onset temperature and T_g (tan δ) is the lowest compared to the other binders. The binders K-140 and D 2433E result in a linear drop in tensile strengh and modulus with increasing content. The partially soluble polyester binder D 2433E shows slightly weaker performance than the nonsoluble polyamide binder K-140. This observation applies to all mechanical parameters investigated here. From these results it can be assumed that binders like Grilon MS, which are strongly soluble in the resin matrix after processing at higher temperatures (but at most partially soluble during infusion processess at room temperature), are preferable for GFRP prefoming and infiltration processes. In comparision to the reference system, the absence of resin-binder interfaces here results in unaffected mechanical performance of the resin matrix modified with up to 11 wt% Grilon MS binder. In contrast, the small differences between partially soluble and nonsoluble binders suggest that any presence of interfaces, regardless of degree, strongly controls mechanical performance. It can be assumed that the development of resin-binder interfaces should be avoided to reduce any degrading morphological effects, which increase at higher binder contents as observed here. These results might correspond directly to the mechanical performance of binder-modified GFRP. This would mean that solubility tests and mechanical testing of resin-binder plates might be suggested as simple screening methods for binder preselection, which has to be confirmed.

Moreover, peeling tests were performed to characterize preform properties and correlated with the observations on binder layer formation. Only the binder layer of K-140 exhibits gaps at the lowest binder loading, which were closed at higher binder loadings, corresponding with an increase in peel strength. For the other two binders, Grilon MS and D 2433E, it is observed that the lowest binder loading investigated here already yields maximum peel strength. This observation might be attributed to better wettability of binder and glass fiber sizing. Other effects such as binder migration can be disregarded. Regardless of binder type and loading, all investigated

binders are predominantly located close to the interply surface, indicating only small intraply migration.

In summary, the strongly soluble binder Grilon MS exhibits the best results in mechanical testing of resin-binder plates and is therefore expected to show the best mechanical performance in GFRP. The effect of the binders on the mechanical performance of GFRP will be discussed in a subsequent publication.

ACKNOWLEDGMENTS

The authors wish to thank Dr C. Schilde (Institute of Particle Technology, TU Braunschweig) for laser diffraction measurements and Prof M. Gorywoda (Hochschule Hof) for his contribution to the discussion of the results. In addition we like to thank the companies EMS-Chemie AG (Switzerland), Momentive and DOW Chemical for providing with binder systems and the epoxy resin.

REFERENCES

1. M. Tanoğlu and A.T. Seyhan, *J. Adhes. Adhes.*, **23**, 1 (2003).
2. Cherif, C. (2013): Leichtbau mit Textilverstärkung für Serienanwendungen –Bindermaterialien – Textile Preforms – Verbundbauteile. Verlag Wissenschaftliche Scripten, Dresden.
3. C.H. Shih and L.J. Lee, *J. Compos. Mater.*, **35**, 1954 (2001).
4. J.C. Brody and J.W. Jr. Gillespie, *Polym. Compos.*, **26**, 377 (2005).
5. V. Rohatgi and L.J. Lee, *J. Compos. Mater.*, **31**, 720 (1997).
6. L. Girdauskaite, S. Krzywinski, H. Rödel, A. Wildasin-Werner, R. Böhme, and I. Jansen, *Appl. Compos. Mater.*, **17**, 597 (2010).
7. G. Estrada, C. Vieux-Pernon, and S.G. Advani, *J. Compos. Mater.*, **36**, 2297 (2002).
8. J. Chen, D. Backes, and K. Jayaraman, *Polym. Compos.*, **17**, 23 (1996).
9. C.H. Shih, Q. Liu, and L.J. Lee, *Polym. Compos.*, **22**, 721 (2001).
10. T.K. Tsotsis, *Polym. Compos.*, **30**, 70 (2009).
11. X.S. Yi, Q.F. Cheng, and Z.Z. Liu, *Sci. China Tech. Sci.*, **55**, 2255 (2012).
12. Arnold, M., Stapf, D., Henne, M., Bender, K., Frei, S., Drechsler, K. Improvement of the toughness of epoxy resin systems using thermoplastic binders. Proc. of SEICO 33rd International Conference & Forum, SAMPE Europe Conferences, Paris, 395–400 (2012).
13. J.C. Brody and J.W. Gillespie, *Compos. Mater.*, **18**, 157 (2005).
14. M. Tanoğlu and A.T. Seyhan, *Mater. Sci. Eng.*, **A363**, 335 (2003).
15. M. Tanoğlu, S. Robert, D. Heider, S.H. McKnight, V. Brachos, and J.W. Gillespie, *Int. J. Adhes. Adhes.*, **21**, 187 (2001).